8.05
Peel Test and Interfacial Toughness

Y. WEI
Institute of Mechanics, CAS, Beijing, People's Republic of China
and
J. W. HUTCHINSON
Harvard University, Cambridge, MA, USA

8.05.1 INTRODUCTION

The peel test has been used widely for the mechanical characterization of adhesion phenomena in various applications involving adhesive joining and thin film technology in industries as diverse as the micropackaging and microelectronic industries and the automotive industry. The test received considerable attention for several decades prior to early 2000s and continued to be the subject of intense scrutiny in a wide range of research areas (e.g., Feliu-Baez *et al.*, 2001; Choi and Oh, 2001; Asai *et al.*, 2001; Bundy *et al.*, 2000; Yang *et al.*, 2000; Hulcher *et al.*, 1999; Tanaka *et al.*, 2000; Rahulkumar *et al.*, 2000; Kawabe *et al.*, 2000). Many experimental and theoretical investigations have been performed on interfacial fracture of the film/substrate systems. The effects of the system parameters, such as the peel angle employed, the film thickness, the degree of intrinsic adhesion acting between the materials, the test rate, temperature, etc., on the interfacial adhesion behavior have been studied. In the most straightforward use of the test, it can serve to rank adhesive interfaces. In more fundamental applications, the test is employed as a means of measuring the intrinsic adhesive energy of an interface or an adhesive layer. It is in such attempts where difficulties often arise due to the occurrence of extensive plasticity that significantly contributes to the experimentally measured effective adhesion energy. An effective partitioning of the intrinsic adhesive energy and the extrinsic plastic dissipation provides the motivation underlying the analyses reviewed in this chapter. Peel test analysis attempts to predict the tensile stresses set up in the adhesive layer in terms of the measured peel force and material properties. Following this line, Spies (1953) was the first to analyze elastic peeling by considering the 90° peeling of a thin strip and the attached part of the adherend as an elastic beam on an elastic (Winkler) foundation with the detached part of the beam undergoing large deformation (an elastica). Similar elastic models have also been presented by Bickerman (1957), Kaeble (1959, 1960), Jouwersma (1960), Yurenka (1962), Gardon (1963), Saubestre *et al.* (1965), Kendall (1973), Gent and Hamed (1975), Nicholson (1977), and Bigwood and Crocombe (1989). The effect of adherend plasticity was considered by Chen and Falvin (1972), Chang *et al.* (1972), Gent and Hamed (1977), and Igarashi (1984). Chen and Falvin (1972) obtained an approximate solution for the peel stress in the presence of adherend plastic deformation. Gent and Hamed (1977) and Igarashi (1984) adopted approximate methods to estimate adherend plastic dissipation based on elementary beam theory. A numerical analysis of elastic–plastic peeling was performed by Crocombe and Adams (1981, 1982), who used the finite element (FE) method to calculate the stress distribution ahead of an interfacial crack. Atkins and Mai (1986) studied the influence of residual strain energy on elastic–plastic peeling. Kim and Kim (1988), Kim and Aravas (1988), and Kim *et al.* (1989) systematically studied the elastic–plastic steadily peeling problem and provided detailed analysis of what will be referred to here as the beam bending model (BB model). They took into account elastic unloading and reversed plastic bending of the strip and obtained estimates of plastic dissipation contribution to the total steady-state work of fracture. Their expressions provided relations among the peel force, adherend properties, and rotation at the root of the detached film. Their results showed that the plastic dissipation could often make a large contribution to the total fracture energy and depended strongly on the root rotation. Underlying the BB model are the standard assumptions of simple beam theory. In particular, the stress state at every point in the beam producing the plastic deformation is uniaxial (or plane strain tension for a wide strip). Using the BB model, Williams (1993), Kinloch *et al.* (1994), and Moidu *et al.* (1995, 1998) modeled the attached part of a flexible adherend as an elastic–plastic beam on an elastic foundation and calculated the crack-tip slope angle and plastic dissipation. They analyzed the role of root rotation due to the adherend compliance. In their analysis, it was assumed that the adherend behaves elastically, although elastic–plastic behavior was taken into account for the attached part of the adherend. Kinloch *et al.* (1994) used this approach to study the peeling of laminated materials. Park and Yu (1998) and Park *et al.* (1999) made an X-ray analysis and experimental study of the peel test for a Cu/Cr/polyimide system. The plastic strain in the peeled metal films and the interfacial fracture energy were measured.

Linear elastic fracture mechanics has been proved to be a useful tool theoretically and

experimentally for assessing the interface fracture behavior and fracture toughness when the adherends are elastic materials (Rice, 1988; Hutchinson and Suo, 1992). By considering the energy balance, one can set up the relation between applied work and the interfacial fracture work, while the applied work can be directly calculated from the solutions of the elastic boundary value problems. In an elastic problem, stress intensity factors are used and critical values of these factors are simply related to the work of fracture. Correspondingly, experimental methods for assessing the fracture behavior of materials or materials-bonded interfaces have been developed accompanying the theoretical advances (Evans *et al.*, 1988; Suga *et al.*, 1988; Argon *et al.*, 1989; Wang and Suo, 1990; Thouless, 1990).

For the peel test under elastic conditions, the peel force per unit width is a direct measurement of the adhesive fracture energy, characterizing the interfacial toughness of adhesive (Kinloch, 1987). Throughout this chapter, the notion of elastic conditions in the peel test will recognize inevitable nonlinearity, including small amounts of plasticity, which accompanies the fracture process and which contributes to the intrinsic adhesion energy of a particular interface. The plasticity occurring outside the fracture process region is the extrinsic plasticity. When the adherends, film, and substrate, or at least one of these, are ductile materials and the interface is sufficiently tough, extrinsic plastic deformation is inevitable. As in the case of conventional elastic–plastic crack growth problems, the interface fracture process zone in the peel test will be shielded extensively due to the plastic deformations. When the adherend undergoes the plastic deformation and unloading process, the peel force per unit width characterizes the total energy dissipated in the system, both the extrinsic plastic dissipation in the adherends and the interface separation energy (or adhesive energy).

Within the framework of elastic–plastic fracture mechanics, an embedded process zone (EPZ) model has been developed (Needleman, 1987; Tvergaard and Hutchinson, 1992, 1993) to analyze the complex interaction between the work of the fracture process and the extrinsic plasticity. The model embeds a cohesive zone within an elastic–plastic continuum. The cohesive zone is specified by a traction–separation law, which is characterized by a work of separation per unit area and a peak separation stress. When applied to a steadily growing crack problem, this approach enables the total energy to be separated into two parts: intrinsic separation energy (the work of the fracture process) and the plastic dissipation due to plastic deformation and unloading in the region surrounding the embedded cohesive zone. Wei and Hutchinson (1998) and Yang *et al.* (1999) have used the EPZ model to analyze peel test problems. A large contribution to the total fracture energy from the plastic dissipation was displayed in their results for sufficiently tough interfaces or, equivalently, for one of the adherends having sufficiently low yield strength. Other interfacial models have been proposed that are also able to capture some of these features, such as the plasticity-free strip model (SSV model) of Suo *et al.* (1993) and Beltz *et al.* (1996), and the unified model of Wei and Hutchinson (1999). In this chapter attention is limited to the EPZ model.

It has been an accepted conclusion that, when film is a ductile material, the total energy of the system consists of the interfacial adhesion energy plus the film plastic dissipation. As mentioned above, there have been a number of research efforts to predict plastic dissipation using the BB model (Kim and Kim, 1988; Kim and Aravas, 1988; Kim *et al.*, 1989). From the BB model, the plastic dissipation comes entirely from the plastic bending and the accompanying elastic unloading and reversed bending in the film. Contributions to the plastic deformation arising from the high stresses occurring near the interface crack tip cannot be resolved by the beam model, and for all practical purposes the BB model neglects this contribution to the plastic dissipation. In most problems of crack growth in ductile solids, the near-tip plasticity is the major source of the plastic dissipation. The peel test is unusual in that plastic dissipation occurs both in the vicinity of the crack tip and well away from the tip due to bending. In fact, the BB model does not account for shielding of the crack tip by plasticity generated by the high local stresses. Wei and Hutchinson (1998) adopted a hybrid analysis that couples a general plane analysis (the GPA model with an embedded cohesive zone) to analyze the attached portion of the film with a beam analysis similar to that used in the BB model to account for behavior in the detached portion of the film away from the tip. The goal is a model capable of partitioning the work of fracture of the interface from the plastic dissipation by accounting for both bending plasticity and plasticity generated near the point where the film separates from the substrate.

The primary objective of this chapter is to compare and contrast the two types of models, the BB model and the hybrid GPA/BB model. In doing so, the issue of whether it is feasible to

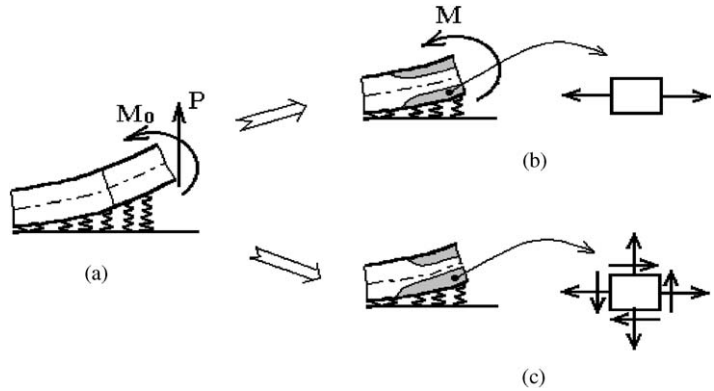

Figure 1 Peel test analytical models for attached film (a), the BB model (b), and the general plane analysis model (c).

partition the work of interface separation from extrinsic plasticity will be in the forefront. In both models, the same cohesive zone representation (EPZ) will be used. In the interests of brevity, the two types of models will be referred to in the chapter as the BB model and the GPA model. A schematic of each of the models is sketched in Figures 1(b) and (c). Using the same methods, attention will also be directed at a new test method, the split test (Wei, 2002), which has much in common with the peel test. An overview of description of the peel test and interfacial toughness is given in Section 8.05.2. The GPA model will be introduced and analyzed in Section 8.05.3. The parallel study of the BB model is presented in Section 8.05.4. The split test is introduced and analyzed in Section 8.05.5. Conclusions, limitations of the models, and recommendations for further work are presented in Section 8.05.6.

8.05.2 PEEL TEST AND INTERFACIAL TOUGHNESS

8.05.2.1 Overview

The peel test is a seductively simple experimental method by which one attempts to measure the interface toughness of a film/substrate system. When the adherends (film and substrate) are elastic materials and the film undergoes steady-state peeling, it is universally agreed that the experimentally measured peel force per unit film width is directly related to the work of fracture of the interface, as detailed below. Assuming the strain energy per unit area in the straight portion of the detached film is much smaller than the peel force per unit width (which is almost always the case), the work done by external force is equal to the work of the interface separation. However, when one or both of the joined materials undergo plastic deformation during steady-state peeling, the peel force per unit width equals the sum of the interface fracture energy and the plastic dissipation. For many systems, the plastic dissipation can be much larger than the interface fracture energy. When this is the case, interpretation of peel test results becomes difficult. For example, while the peel force for an elastic system is independent of the film thickness, it can depend strongly on the thickness when significant plasticity occurs, clouding the interpretation of the test. The primary goal of the peel test analyses presented here is to elucidate the partitioning of the work of separation (or, equivalently, the adhesion energy) and the plastic dissipation.

8.05.2.2 Elastic Peeling and Energy Balance

The peel test geometry is sketched in Figure 2(a). In an elastic peeling process, both adherends undergo the elastic deformation, apart from inelasticity, including plasticity, i.e., inseparable from the fracture process. Let Γ_0 be work of separation (energy per unit area of interface). In steady-state peeling the work done by the external force per unit width, P, per unit length of interface debonding is $P(1-\cos\Phi)$, where Φ is the peel force direction angle. The ratio of the strain energy in the film per unit area remote from the crack tip to Γ_0 is $P/2Et$ where t is the film thickness. If this ratio is small compared to unity, essentially all the work of the peel force is consumed by the fracture process such that

$$P(1-\cos\Phi)=\Gamma_0 \tag{1}$$

In an elastic steady-state peel test, the interfacial toughness (adhesion energy) Γ_0 can be obtained by measuring the peel force and the direction in which it acts.

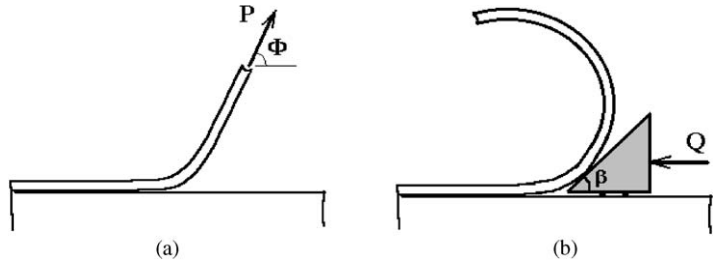

Figure 2 Two test methods: (a) the peel test, and (b) the split test.

8.05.2.3 Elastic–Plastic Peeling and Energy Balance

When the film undergoes plastic loading, elastic unloading, and reversed plastic loading during steady-state peeling, the energy stored in the peeled film per unit area of crack advance, Γ^{p}, is equal to the difference between the upstream and downstream energies per unit area. The work done by the peel force per unit crack advance is still equal to $P(1-\cos\Phi)$, and the interface fracture energy per unit of interface debond area is Γ_0. The energy balance requires

$$P(1-\cos\Phi) = \Gamma_0 + \Gamma^{p} \tag{2}$$

Usually, Γ^{p} is called the plastic contribution to the total work of fracture. In the peel test, the contributions to Γ^{p} arise in the general vicinity of the crack tip where the crack-tip stresses are the highest and somewhat downstream from the tip due to bending and reversed bending.

8.05.2.4 Elastic–Plastic Split Test

The split test (Figure 2(b); Wei, 2002) has much in common with the peel test, with both relative advantages and disadvantages. In the split test, two measurable parameters are featured: the residual curvature κ_0 and the split force Q. During steady-state splitting, the film is subject to a wedge force at a fixed location relative to the crack tip. The film undergoes a sequence of processes from elastic–plastic deformation and unloading ending in an unloaded state with a constant residual curvature. The detached film behind the wedge rolls up into a circular hoop due to residual stresses. Under ideal circumstances, by measuring the residual curvature of the circular hoop and the split driving force in the test, one can obtain the interfacial fracture toughness for the film/substrate system. In the split test, under steady-state splitting, the energy balance implies

$$Q = \Gamma_0 + \Gamma^{p} + \Gamma^{f} \tag{3}$$

where Q is the split force per unit width, Γ^{p} is the plastic dissipation per unit area in the split arm, and Γ^{f} is frictional dissipation per unit area on the contact faces between the splitter head and the film surfaces. Under conditions of frictionless contact, $\Gamma^{f}=0$. In Section 8.05.5, an analysis is presented that makes use of the measured residual curvature of the split film to estimate Γ^{p} and, therefore, to deliver the interfacial toughness Γ_0 to be obtained.

8.05.3 PEEL TEST ANALYSIS BASED ON THE GENERAL PLANE ANALYSIS AND THE EPZ MODEL

In this section, the GPA model with an embedded cohesive zone is used to analyze the steady-state peel test. As described previously, the GPA model is a hybrid combination of a FE model to resolve stress and strains of the attached film in the region where it detaches from the substrate and a BB model to account for plasticity that occurs in subsequent bending and reversed bending. It is assumed that the film is wide compared to its thickness and, therefore, a plane strain model is adopted. Much of the content in this section is taken from Wei and Hutchinson (1998), although that study did not bring out the important role of the yield stress to modulus ratio of the film that will be emphasized here.

8.05.3.1 The Interface Traction–Separation Relation (EPZ Model)

The thickness of the interface in the unloaded state is taken to be zero. Following the notation for the interface traction–separation relation introduced in Tvergaard and Hutchinson (1992, 1993) and in Wei and Hutchinson (1998), let δ_n and δ_t be the normal and tangential components of the relative displacement of the respective faces across the interface in the zone where the separation process occurs, as indicated in Figure 3. Let δ_n^c and δ_t^c be critical values of these displacement components, and define a single dimensionless

separation measure as

$$\lambda = \sqrt{(\delta_n/\delta_n^c)^2 + (\delta_t/\delta_t^c)^2} \tag{4}$$

such that the tractions drop to zero when $\lambda = 1$. With $\sigma(\lambda)$ displayed in Figure 3, a potential from which the interface tractions in the separation zone are derived is defined as

$$\Pi(\delta_n, \delta_t) = \delta_n^c \int_0^\lambda \sigma(\lambda')\mathrm{d}\lambda' \tag{5}$$

The normal and tangential components of the traction acting across the interface in the fracture process zone are given by

$$\begin{aligned} T_n &= \frac{\partial \Pi}{\partial \delta_n} = \frac{\sigma(\lambda)}{\lambda}\frac{\delta_n}{\delta_n^c}, \\ T_t &= \frac{\partial \Pi}{\partial \delta_t} = \frac{\sigma(\lambda)}{\lambda}\frac{\delta_t}{\delta_t^c}\frac{\delta_n^c}{\delta_t^c} \end{aligned} \tag{6}$$

The traction law under a purely normal separation ($\delta_t = 0$) is $T_n = \sigma(\lambda)$ where $\lambda = \delta_n/\delta_n^c$. The peak normal traction under purely normal separation is $\hat{\sigma}$, which will be termed the interface strength. Under a purely tangential displacement ($\delta_n = 0$), $T_t = (\delta_n^c/\delta_t^c)\sigma(\lambda)$ where $\lambda = \delta_t/\delta_t^c$. The peak shear traction is $(\delta_n^c/\delta_t^c)\hat{\sigma}$ under a purely tangential displacement of the faces. The work of separation per unit area of interface Γ_0 is given by Equation (5) with $\lambda = 1$. For the separation function $\sigma(\lambda)$ specified in Figure 3,

$$\Gamma_0 = \tfrac{1}{2}\hat{\sigma}\delta_n^c(1 - \lambda_1 + \lambda_2) \tag{7}$$

The separation law is assumed to be independent of the time rate of deformation, as are the constitutive models characterizing the film and substrate. The parameters governing the separation law of the interface are the work of the fracture process Γ_0, the peak stress quantity $\hat{\sigma}$, and the critical displacement ratio δ_n^c/δ_t^c, together with the factors λ_1 and λ_2 governing the shape of the separation function. The potential function ensures that the work of separation is Γ_0 regardless of the combination of normal and tangential displacements taking place in the separation of the interface. Experience gained in the earlier studies suggests that details of the shape of the separation law are relatively unimportant. The two most important parameters characterizing interface separation are Γ_0 and $\hat{\sigma}$. The dimensionless parameter δ_n^c/δ_t^c is the next most important, but the study of mixed mode interface toughness (Tvergaard and Hutchinson, 1993) indicates that predictions are relatively insensitive to this parameter as long as the interface process is dominantly normal separation. This is the case for the peel test under the range of peel angles considered here.

Attainment of $\lambda = 1$ at the end of the traction–separation zone (the point of separation) is the condition for crack advance. In steady-state propagation, this condition must be imposed on the solution.

8.05.3.2 The GPA/EPZ Model for Steady-state Peeling

The geometry of the model is displayed in Figures 3 and 4 with a peel angle Φ. Plane strain conditions are assumed, as appropriate for a film whose width normal to the plane of deformation in Figures 3 and 4 is sufficiently large compared to its thickness t. Except for an example of an elastic film peeling from an elastic–plastic substrate presented at the end of Section 8.05.3, the film is taken to be elastic–plastic with Young's modulus E, Poisson's ratio ν, tensile yielding stress σ_Y, and strain hardening exponent N. Rate-independent material behavior is assumed. The substrate is elastic with modulus E_s and Poisson's ratio ν_s. The standard J_2 flow theory of plasticity, based on the von Mises yield surface, is used to characterize plasticity in the film. The small strain version of the theory is employed,

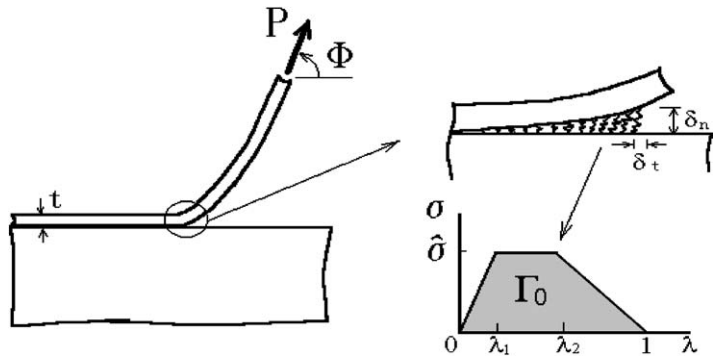

Figure 3 The peeling process characterized by the EPZ model.

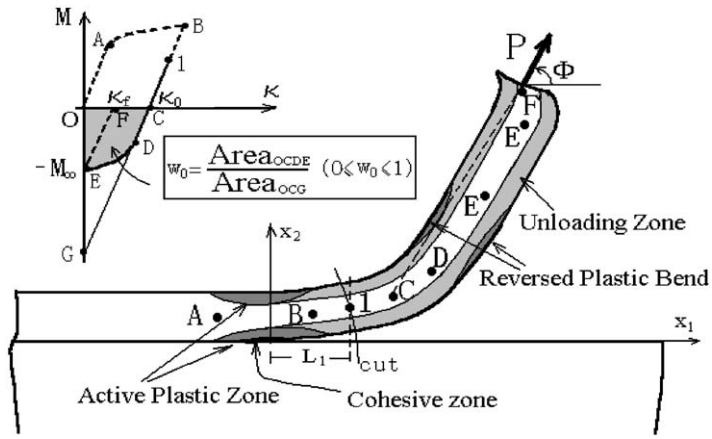

Figure 4 The mechanics behavior of a peeled film with conventions for modeling.

consistent with the fact that the strains and rotations in the films attached to the substrate and near the tip of the steadily growing crack are indeed small under steady-state conditions. The tensile stress–strain relation used to characterize the film material is

$$\sigma = \begin{cases} E\varepsilon, & \text{if } \sigma \leq \sigma_Y \\ \sigma_Y(\varepsilon/\varepsilon_Y)^N, & \text{if } \sigma \geq \sigma_Y \end{cases} \tag{8}$$

The interface crack is assumed to have propagated a sufficient distance such that steady-state conditions prevail in the vicinity of the propagating interface crack (Hutchinson, 1974). In Figure 4, the interface propagates to the left. Where the plastic strain rate $\dot{\varepsilon}_{ij}^{p}$ is nonzero dark shading depicts the active plastic zone. Light shading shows zones behind the advancing tip that have unloaded but contain residual plastic strains. Zones of reversed plastic loading generally will occur at some distance from the crack tip in the detached film strip (Kim and Aravas, 1988; Kinlock *et al.*, 1994). Dark shading also depicts these.

The peel angle Φ specifies the angle that the peel force per unit width of film P makes with the plane of the interface. Let $M(s)$ be the bending moment (per unit width) about the middle plane of the separated film at a distance s along the film measured from the crack tip. The origin of the coordinate system (x_1, x_2) is at current location of the tip where $\lambda = 1$. For analysis purposes, the problem is subdivided into two parts (cf. Figure 4): the substrate plus the film to the left of $s = x_1 = L_1$, and the separated infinite film segment to the right of L_1. Wei and Hutchinson (1998) have argued that accurate results from the cohesive zone model require a full 2D plane strain, continuum analysis of the behavior in the vicinity of the interface crack. Representation of the film and substrate by a BB model of the film is unable to capture the highly nonuniform stress and strain distributions in the vicinity of the separation zone and will miss essential features of the separate-ion phenomena. For example, a BB model cannot capture the small-scale yielding limit based on the stress singularity when the active plastic zone is confined to a region near the crack tip. An Eulerian-based FE formulation designed to cope with steady-state conditions will be employed. The point at $s = L_1$ is where the full 2D continuum analysis of the crack-tip problem is matched to a 1D bending problem for the separated film strip. This point must lie to the right of the active plastic zone at the crack tip and to the left of any reversed plastic bending. Otherwise, the location of this matching point will be seen to have essentially no effect on the solution as long as the slope θ_1 there is small. The term GPA refers to the coupled two-segment analysis.

The film that emerges from the region to the left of L_1 has been subject to plastic deformation and has a residual curvature κ_0 prior to any reversed plastic deformation. The film at the matching point $s = L_1$ has undergone elastic unloading sustaining a moment M_1 less than the maximum moment, which is attained at some point to the left of L_1. The moment–curvature relation of the film emerging into the region to the right of L_1 is displayed as the unloading branch in Figure 4. The initial portion of the curve of M vs. κ is shown dashed since it is not used in the analysis. (This is the portion of the behavior computed using the full 2D representation of the film.) Reversed plastic deformation, if it occurs, takes place when M becomes sufficiently negative (Kim and Kim, 1988; Kim and Aravas, 1988; Kinlock *et al.*, 1994). At a distance s far from the tip, the film becomes straight, corresponding to the state $M = -M_\infty$ with $\kappa = 0$. The final residual curvature of the unloading film ($M = 0$) is labeled in Figure 4 as

κ_Γ. For the purpose of comparison with the BB model in the next section, the residual curvature κ_0 emerging from the crack-tip region prior to reversed plastic bending is computed as part of the solution to the peel test problem and presented.

Plastic deformation due to reversed plastic bending contributes to the overall rate of plastic work in the system, and it reduces the final residual curvature of the film from the value, κ_0, inherited from the plastic deformation in the vicinity of the interface crack tip. Reversed plastic deformation depends on the Bauschinger behavior of the material, which is not well quantified by conventional yield surface descriptions, and especially not by an isotropic hardening theory. Because reversed plastic deformation occurs in the segment of the problem, i.e., well characterized by 1D nonlinear bending theory, full details of the plastic constitutive behavior under reversed loading need not be considered. It will be shown that only the normalized shaded area w_0 under the overall moment–curvature relation of the film in Figure 4 matters in the final results.

The study of Wei and Hutchinson (1998) followed in this section considered the following parameters:

$$\begin{aligned} &E,\ \nu,\ \sigma_Y,\ N,\ t\ (\text{film}); \qquad E_s,\ \nu_s\ (\text{substrate});\\ &\Gamma_0,\ \hat{\sigma}\ (\text{interface}). \end{aligned} \tag{9}$$

The substrate was assumed to undergo only elastic deformations. In a later subsection, plasticity in the substrate will be considered. The peel angle Φ and the work per unit width of film w_0 characterizing reversed plastic bending complete the parameter set. An additional variable, which is likely to have a major influence on the peel force, is residual stress in the attached film acquired in the bonding process. When the residual stress is a nonnegligible fraction of the yielding stress, it will alter plastic dissipation in subsequent peeling. Residual prestress can be included in the GPA model, but it will not be considered here in the interest of reducing the number of variables.

The following material-based length quantity plays a fundamental role in the solution

$$R_0 = \frac{1}{3\pi(1-\nu^2)}\frac{E\Gamma_0}{\sigma_Y^2} \tag{10}$$

The extent of the plastic zone scales with R_0. When P is only slightly larger than Γ_0, this length can be regarded as an estimate of the plastic zone height in the film at the crack tip (Tvergaard and Hutchinson, 1992, 1993, 1994). In general, however, R_0 is less than the plastic zone height and should simply be regarded as a fundamental parameter with dimensions of length. The same length quantity (apart from a numerical constant) emerges as fundamental in the analysis of Kim and Kim (1988) and Kim *et al.* (1989). Dimensional considerations dictate that the solution for the peel force P must have the general nondimensional form

$$\begin{aligned} &\frac{P(1-\cos\Phi)}{\Gamma_0}\\ &= F\left\{\frac{t}{R_0},\ \frac{\hat{\sigma}}{\sigma_Y},\ N,\ \Phi,\ \frac{\sigma_Y}{E},\ \frac{E_s}{E},\ \nu,\ \nu_s\right\} \end{aligned} \tag{11}$$

where F is dimensionless. When elastic peeling conditions pertain, $F = 1$. Implicit in this dependence are details of the hardening rule for reversed plastic straining, e.g., isotropic vs. kinematic hardening. The number of dimensionless variables in any mechanics model of the peel test is large, even when any residual stress arising during bonding is ignored. To reduce the number of variables, Wei and Hutchinson (1998) took $\nu = \nu_s = 0.3$, and assumed either no elastic mismatch ($E_s = E$) or a highly compliant film on a stiff substrate with $E = E_s/100$. The shape parameters in the traction–separation law were taken to be $\lambda_1 = 0.15$ and $\lambda_2 = 0.5$, while δ_n^c/δ_t^c is fixed at unity, following earlier studies of Tvergaard and Hutchinson. Of the remaining dimensionless variables in Equation (11), t/R_0, $\hat{\sigma}/\sigma_Y$, N, σ_Y/E, and Φ all have significant influence on $P(1-\cos\Phi)/\Gamma_0$ when plastic dissipation is nonnegligible. In earlier work on interface fracture of two thick substrates separated by a ductile layer (Tvergaard and Hutchinson, 1994) or of interface fracture of a prestressed ductile film on a thick substrate (Wei and Hutchinson, 1997a), the effect of the yield stress primarily entered through t/R_0 with little additional dependence on σ_Y/E. However, for the peel test, because of the susceptibility of the film to plastic bending as well as near-tip plasticity, the yield stress has a strong role through both of these dimensionless parameters and the separate role of σ_Y/E will be featured.

Results presented as $P(1-\cos\Phi)/\Gamma_0 = F$ represent the ratio of the total work of peeling to the work of the separation process, or, equivalently, by (2), $1 + \Gamma^p/\Gamma_0$. Thus, the extent to which this ratio exceeds unity reflects the relative contribution of the plastic dissipation to the total work of fracture.

8.05.3.3 Formulation and Numerical Solution

The two parts of the problem in Figure 4 are analyzed separately and coupled by requiring continuity of force, moment, displacement, and

rotation at $x_1 = L_1$. The first part to the left of L_1 is analyzed as a steady-state, plane-strain continuum problem employing a special iterative scheme briefly mentioned below. The second part to the right of L_1 is treated as a finite rotation, bending problem (an elastic–plastic "elastica") with a residual curvature κ_0 arising from plastic deformation in the first part. The analysis of each part is described, followed by a prescription of the coupling conditions.

8.05.3.3.1 FE solution for $x_1 \leq L_1$

The incremental relation between the stress and strain in the J_2 flow theory of plasticity is

$$\dot{\sigma}_{ij} = D_{ijkl}\dot{\varepsilon}_{kl} \tag{12}$$

where elastic–plastic modulus tensor can be expressed as

$$D_{ijkl} = \frac{E}{1+\nu}\left\{\delta_{ik}\delta_{jl} + \frac{\nu}{1-2\nu}\delta_{ij}\delta_{kl} - \frac{(3/2)\Omega}{[1+(2/3)(1+\nu)H/E]\sigma_e^2}\sigma'_{ij}\sigma'_{kl}\right\} \tag{13}$$

Here σ'_{ij} is the stress deviator, $\sigma_e = \sqrt{3\sigma'_{ij}\sigma'_{ij}/2}$ is the effective stress, $\Omega = 1$ for plastic loading and vanishes otherwise, and H is plastic hardening modulus. For the power-law strain hardening case (see Equation (8)), one has

$$H = E\left[\left(\frac{1}{N}\right)\left(\frac{\sigma_e}{\sigma_Y}\right)^{1/N-1} - 1\right]^{-1} \tag{14}$$

The emphasis here is on the steady-state growth wherein the crack has advanced sufficiently far from initiation such that stresses and strains no longer change from the vantage point of an observer translating with the crack tip (Hutchinson, 1974). The crack problem is posed for steady-state crack growth under constant driving force P. A zone of active plasticity moves with the crack tip and a wake (or unloading) of plastically deformed, but elastically unloaded, material extends to the right, as depicted in Figure 4. Downstream, the stresses and strains well ahead of the advancing interface crack tip $(x_1 \to -\infty)$ vanish because residual stresses in the film are assumed to be absent. In the small strain, small rotation steady-state problem, the rate at any point of a quantity such as stress and strain is related to the leftward velocity V of the crack tip and the gradient in x_1-direction by

$$(\dot{\sigma}_{ij},\ \dot{\varepsilon}_{ij}) = V\left(\frac{\partial\sigma_{ij}}{\partial x_1},\ \frac{\partial\varepsilon_{ij}}{\partial x_1}\right) \tag{15}$$

where V is the leftward velocity of the crack tip. Substituting the steady-state formula (15) into the rate-independent incremental constitutive relation (12), a partial differential equation for stress and strain to x_1 in the form

$$\frac{\partial\sigma_{ij}}{\partial x_1} = \frac{D_{ijkl}\partial\varepsilon_{kl}}{\partial x_1} \tag{16}$$

is obtained, which is independent of V.

It is the above feature that makes it possible to directly solve the problem without having to consider transient behavior preceding attainment of steady state. Dean and Hutchinson (1980) and Parks *et al.* (1981) developed the Eulerian-based solution scheme. It was applied to the related studies of steady-state thin film delamination, thin film peeling, and cracking by Wei and Hutchinson (1997a, 1998, 1999). Wei and Hutchinson (1998) present a detailed outline of the solution method. The numerical procedure requires integration along stream lines to obtain the history of the stress and plastic strain at any point in the field. Moreover, iteration is required to ensure that the conditions of steady state are met at every point in the field. The FE procedure employed an equal-height mesh specially designed for the regions around the crack surface near the crack tip to cope with the steady-state wake and the stream-line integration. Most of the numerical results presented below are taken from Wei and Hutchinson (1998), who used eight noded isoparametric elements with four Gauss integration points in each element.

8.05.3.3.2 Solution in the film for $x_1 > L_1$

Within the first part, the film emerges from the active plastic zone with a plastic strain $\varepsilon^p_{ij}(x_2)$ that depends on x_2 but is independent of x_1. This is the state inherited by the film segment to the right of L_1. If the film were unloaded prior to any reversed plastic bending, it would have a residual curvature κ_0 given by

$$\kappa_0 = -\frac{12}{t^3}\int_0^t \left(x_2 - \frac{1}{2}t\right)\varepsilon^p_{11}(x_2)\mathrm{d}x_2 \tag{17}$$

As noted earlier, reversed plastic deformation further to the right of L_1 will reduce the final residual curvature of the unloaded peeled film to κ_f.

The film segment to the right of L_1 is modeled as an in-extensional elastic–plastic "elastica," following several earlier approaches. The present outline is taken from Wei and Hutchinson (1998). In the segment to the right of L_1, the relation of moment per unit

width M and the curvature κ is of the form shown in Figure 4. During unloading prior to reversed plastic bending, $M = B(\kappa - \kappa_0)$, where $B = Et^3/[12(1-\nu^2)]$ is the elastic bending stiffness per unit width of the film. With s as the distance along the film middle surface measured from the tip, and with θ as the rotation of the film middle surface relative to the x_1-axis, $\kappa = \mathrm{d}\theta/\mathrm{d}s$. Equilibrium requires $\mathrm{d}M/\mathrm{d}s = -P\sin(\Phi - \theta)$. Use $\kappa = \mathrm{d}\theta/\mathrm{d}s$ and integrate the equilibrium equation from $M = -M_\infty$, where $\theta = \Phi$ and $\kappa = 0$, to M to obtain the connection between M_1 and θ_1 at the point $s = L_1$ (Figure 4):

$$M_1 = B\kappa_0\left\{\left[(1-\cos(\Phi-\theta_1))\left(\frac{2P}{B\kappa_0^2}\right) + 1 - w_0\right]^{1/2} - 1\right\} \tag{18}$$

where $w_0 = 2W_0/B\kappa_0^2$. In this form, which is due to Wei and Hutchinson (1998), it can be seen that the relation between M_1 and θ_1 (which is an exact integration of the nonlinear elastic–plastic bending equation) depends on reversed plastic bending only through the area ratio w_0. As $B\kappa_0^2/2$ is the area below the κ-axis in Figure 4 in unloading elastically to $\kappa = 0$, w_0 provides a measure of the effect of reversed plastic bending. It will be unity if no reversed plastic bending occurs. Smaller values of this ratio are pertinent when peeling involves significant plastic deformation. The quantity w_0 can be computed for any specific stress–strain description for reversed stressing. However, given the variety of plasticity descriptions for reversed stressing and the lack of agreement on which constitutes the best choice, we prefer to follow the earlier work of Wei and Hutchinson and retain w_0 as an independent parameter.

8.05.3.3.3 *Coupling of two parts of the solution at* $x_1 = L_1$

Continuity of displacement, rotation, force, and moment is required at the point $s = x_1 = L_1$ where two parts of the solution are matched. For the problem of the first part, a linear distribution of tractions is applied to the film along $x_1 = L_1$ with resultants chosen to coincide with the horizontal and vertical components of the force per unit width ($P\cos\Phi$, $P\sin\Phi$) and the moment per unit width M_1. The rotation θ_1 in the first part is computed as the rotation of the centerline of the film at $x_1 = L_1$. The continuity conditions are included in the set of equations to be satisfied in the iterative solution process. Thus, M_1 and θ_1 computed from the first part satisfy Equation (18) at the end of the iteration process.

8.05.3.4 Numerical Results from the GPA Model for Steady-state Peeling

Wei and Hutchinson (1998) performed calculations based on the formulation just described, and selected results from that paper will be presented here. Additional results have been computed and will be presented. These reveal the importance of σ_Y/E as a distinct parameter in the solution set. The results have been selected to bring out the dependence of the normalized peel force, $P(1-\cos\Phi)/\Gamma_0$, on the dimensionless parameters identified in Equation (11). The fraction w_0 measuring the contribution from reversed plastic bending is an additional parameter that will be considered. As emphasized in Section 8.05.3.2, $P(1-\cos\Phi)/\Gamma_0$ represents the ratio of the macroscopic work of fracture to the work of interface adhesion. The extent to which $P(1-\cos\Phi)/\Gamma_0$ exceeds unity reflects the relative contribution of plastic dissipation in the film to the total work of fracture.

8.05.3.4.1 *Normal peel force* ($\Phi = 90^\circ$)

Curves of $P(1-\cos\Phi)/\Gamma_0$ as a function of the normalized film thickness t/R_0 are shown in Figure 5 for a peeling force acting normal to the interface ($\Phi = 90^\circ$). In Figure 5(a) the elastic modulus of the substrate is identical to that of the film, while in Figure 5(b) the substrate is a hundred times stiffer than the film ($E_s/E = 100$). Otherwise, the parameters characterizing the film and the interface are the same in the two plots. The interface is taken to be relatively strong with the interface strength $\hat{\sigma}$ four times the yielding strength of the film σ_Y. The strain-hardening index of the film is $N = 0.1$. The work of interface adhesion Γ_0 enters as the normalization of the peel force P and also in the length parameter R_0 defined in Equation (10). The full range of reversed plastic bending is spanned by the curves in Figures 5(a) and (b).

Recall that $w_0 = 1$ corresponds to no reversed plastic bending. At the other limit $w_0 = 0$, reversed plastic bending occurs as soon as M becomes negative. This latter limit would never be fully attained and would be approached only if the plastic deformation accompanying peeling were large. Suppression of reversed plastic bending has the effect of decreasing the moment carried by the film at the crack tip, thereby requiring a larger peel force to propagate the crack than when reversed plastic

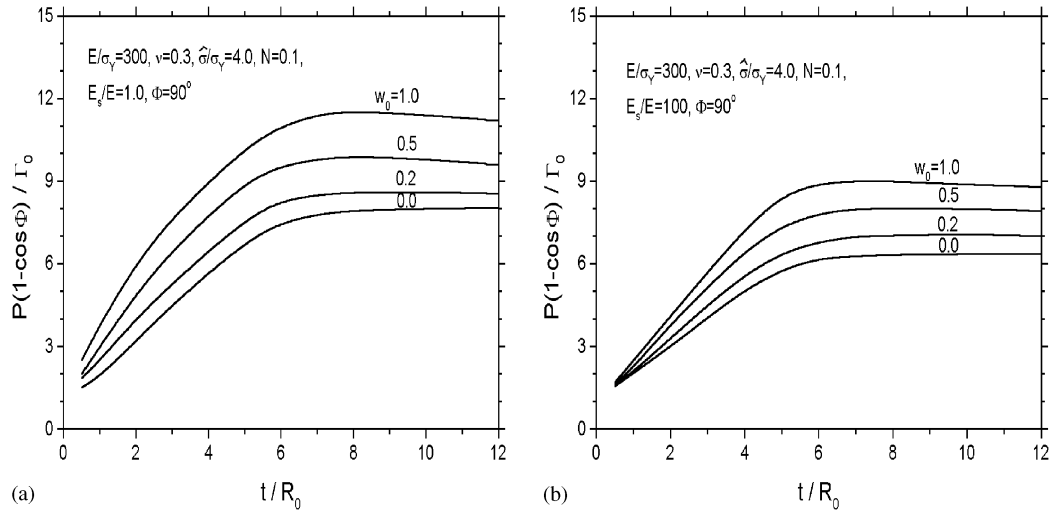

Figure 5 The variations of normalized fracture work with film thickness for several values of w_0: (a) $E_s/E = 1.0$, (b) $E_s/E = 100$.

bending occurs. It is evident from Figure 5 that reversed plastic bending plays some role in determining the peel force, but not a dominant one. Similarly, a stiff substrate reduces the peel force relative to that for a more compliant substrate, but the effect is again subdued.

Wei and Hutchinson (1998) studied the influence of the location $x_1 = L_1$ where the two parts of the solution described in Section 8.05.3.3 are matched by repeating the calculations with different choices of L_1 to test for numerical sensitivity. Since the first part of the solution (the FE solution) is based on a small rotation formulation, it is also essential that θ_1 turns out to be small. The calculations reported here were computed with $L_1/R_0 = 20$. This choice ensures that the matching point is well ahead of the active plastic zone at the crack tip and well to the left of the zone of reversed plastic bending. The angle θ_1 never exceeds 10° and is usually much less than this. Repeating selected calculations such as those shown in Figure 5 for other choices of L_1/R_0, differing by as much as a factor of 2, produced, at most, only a 2% or 3% change in the peel force.

The major trend brought out by Figure 5 is the dependence of the peel force on the film thickness t. Numerical values of $P(1-\cos\Phi)/\Gamma_0$ in Figures 5(a) and (b) have been computed at the values of t/R_0 between 0.5 and 12 (and to even larger values in Figure 16). When t is small compared to R_0, plasticity occurs throughout the film, but plastic dissipation is nevertheless small compared to Γ_0 because the volume of film material is small. The peel test is an unusual illustration of a fracture phenomenon where large-scale yielding is associated with lower toughness than small-scale yielding. In the limit as t goes to zero, P approaches the interface adhesion Γ_0. At the other limit, when t/R_0 is sufficiently large, P/Γ_0 approaches an asymptote. This asymptote corresponds to a small-scale yielding limit in the sense that the active plastic zone is confined to the crack tip, is small compared to the film thickness, and becomes independent of t/R_0. In this limit, there is no yielding on the top surface of the film above the tip and no reversed plastic bending such that $w_0 = 1$. Steady-state toughness in this limit is the same as that for an interface crack in small-scale yielding at the same mode mixity (Tvergaard and Hutchinson, 1993). The trend in Figure 5 from large-scale yielding at small t/R_0 to small-scale yielding at sufficiently large t/R_0 cannot be captured by the BB model since that model does not describe plastic dissipation in the small-scale yielding limit. Detailed comparisons will be made subsequently.

The relatively strong interface ($\hat{\sigma}/\sigma_Y = 4$) gives rise to considerable plastic dissipation such that the total work of fracture is approximately an order of magnitude greater than the work of interface adhesion when the film is sufficiently thick. For normalized interface strengths $\hat{\sigma}/\sigma_Y$ above 4 in Figure 6, the peel force attains a maximum when the normalized thickness is $t/R_0 \approx 6$ for the case $w_0 = 1$. The peak becomes somewhat more prominent at smaller peel angles, as will be seen below. Peel tests on metal films with very strong interfaces and values of P/Γ_0 as large as 100 display a pronounced peak at intermediate film thicknesses (Kim and Kim, 1988). The beam model of Kim and Kim (1988) predicts a peak peel force at roughly comparable values of normalized thickness.

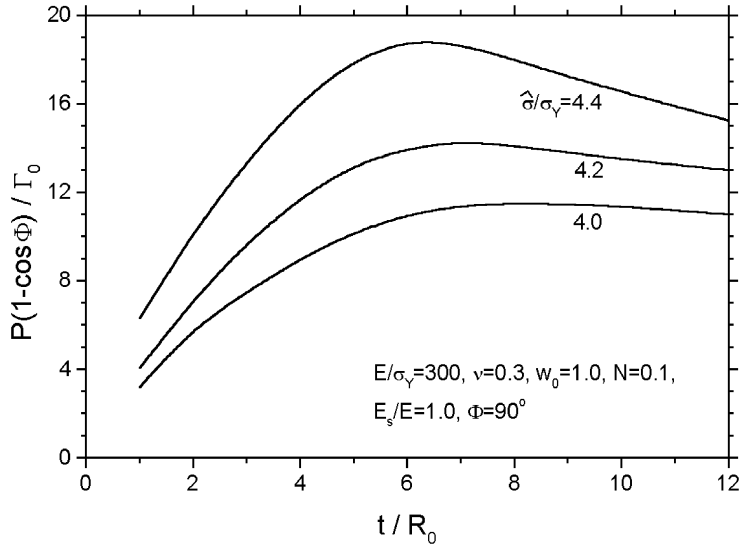

Figure 6 The variations of normalized fracture work with film thickness for several values of interface separation strength.

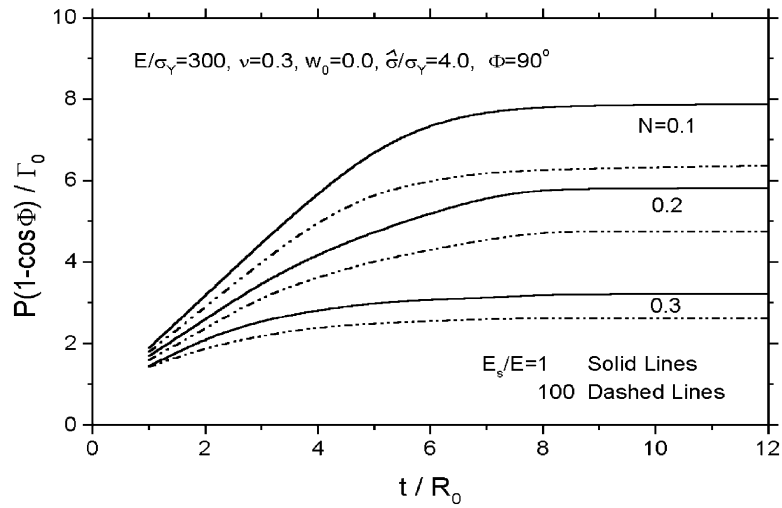

Figure 7 The variations of normalized fracture work with film thickness for several values of strain-hardening index N.

The effect of the strain-hardening index N of the film is displayed in Figure 7 for the case $w_0 = 0$. The other parameters specifying the film/substrate system are the same as those in Figure 5. Strain hardening elevates crack-tip stresses and, accordingly, makes it possible to attain a given interface strength $\hat{\sigma}$ at a reduced peel force. It also increases the moment experienced near the crack tip at a given peel force. The relative effect is the largest for thicker films with the highest levels of plastic dissipation.

In the GPA model of the peel test, the interface strength $\hat{\sigma}$ has very important influence on ratio P/Γ_0, as seen in Figure 8. Curves are shown for two ratios of film to substrate moduli and three strain hardening exponents. The curves are all for the case $w_0 = 0$ and $E/\sigma_Y = 300$, and they are computed with $t/R_0 = 10$ corresponding to films that are sufficiently thick to lie near the asymptotes in Figures 5 and 6. The normalized interface strength $\hat{\sigma}/\sigma_Y$ determines the extent to which the peel force exceeds the interface work of fracture Γ_0. When $\hat{\sigma}/\sigma_Y$ is less than ~ 2, plastic dissipation is nearly negligible compared to Γ_0. Local stress levels at the interface crack tip are low and induce relatively little plastic straining for the yielding stress taking as $\sigma_Y/E = 1/300$. This is the range of interface strengths for which the peel force is essentially the interface work of adhesion for all film thicknesses, except those having very low values of σ_Y/E

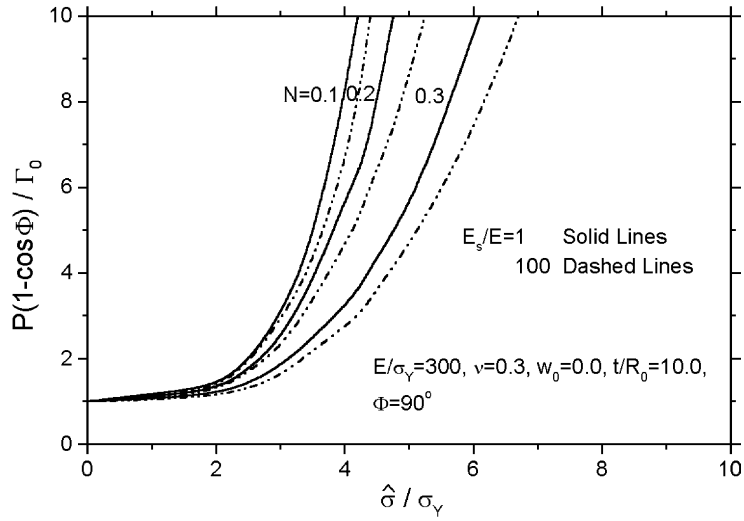

Figure 8 The normalized total work of fracture as a function of the interface separation strength for several cases of N.

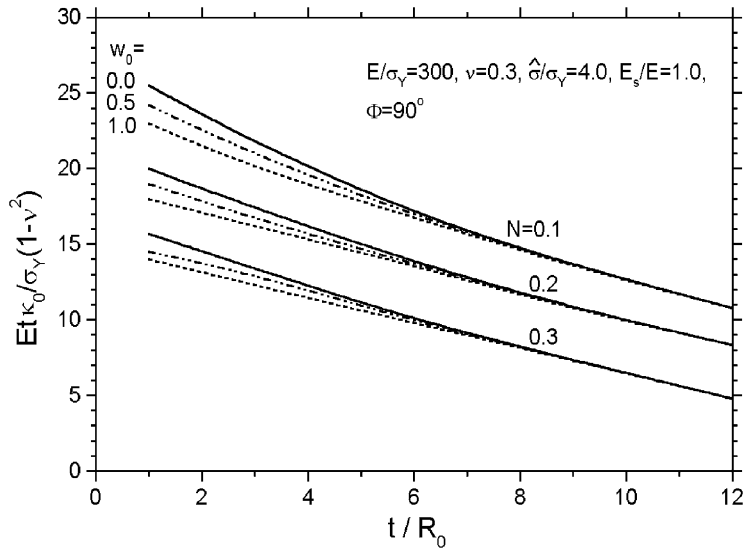

Figure 9 The variations of normalized residual curvature with film thickness for several values of w_0 and N.

(see ahead). Plastic dissipation becomes an increasingly large fraction of the total work of fracture for values of $\hat{\sigma}/\sigma_Y$ larger than 2, depending also on N, or for the yielding stress decreasing, as seen subsequently. As emphasized by Wei and Hutchinson (1998), Figure 8 drives home perhaps the most important qualitative point emerging from the GPA model: the peel force scales with the work of interface adhesion, but the extent to which the peel force exceeds the work of adhesion depends primarily on the normalized interface strength. Qualitatively, these trends are similar to those found by Tvergaard and Hutchinson (1992, 1993) for the ratio of the total work of fracture to the work of the fracture process for mode I crack propagation in homogeneous metals as well as for mixed mode interface fracture under small-scale yielding. In those studies, an embedded fracture process model with the traction–separation law (Equation (6)) was also employed to represent the fracture process on the extended crack plane or on the interface.

To complete the set of results for peeling under a normal force, the residual curvature κ_0 (Equation (17)) emerging from the crack-tip region (and prior to reversed plastic bending) and the opening angle α under load measured at the interface crack tip are presented. Curves of normalized residual curvature $Et\kappa_0/[\sigma_Y(1-\nu^2)]$ as a function of t/R_0 are plotted in Figure 9 for the same set of film/substrate parameters used in plotting Figures 5 and 6. The companion plots for the crack opening angle are given

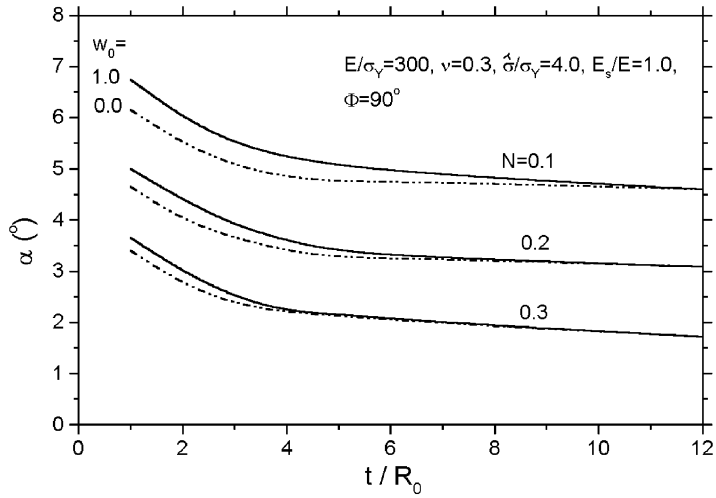

Figure 10 The crack-tip slope angle as a function of the film thickness for several values of w_0 and N.

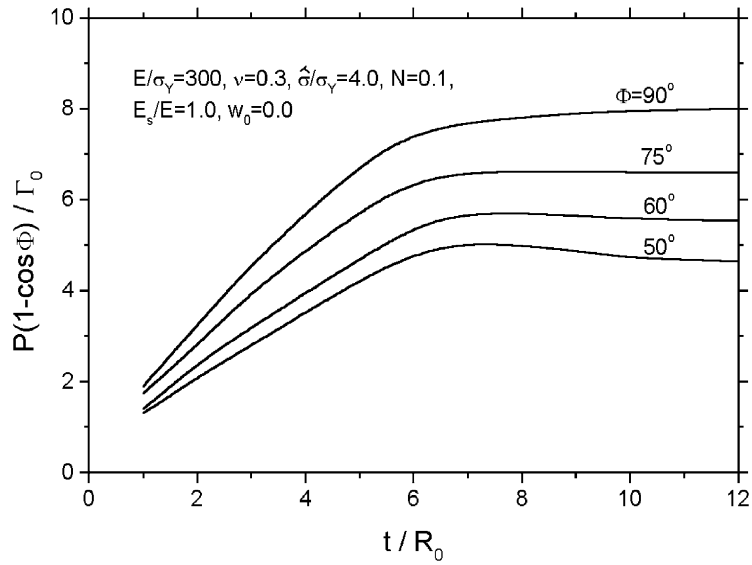

Figure 11 The variations of normalized fracture work with film thickness for several values of peel angles.

in Figure 10. The opening profile of the crack near its tip in steady-state propagation can be closely approximated by the angle that the separated film surface makes with substrate surface, with due account for the fact that the opening displacement at the tip itself is at the critical separation value $\delta_n(0)$ given by the traction–separation law (Equation (6)). An effective definition can be given in terms of the crack face opening $\delta_n(r)$ a small distance r behind the tip according to

$$\tan\alpha = \frac{\delta_n(r) - \delta_n(0)}{r} \qquad (19)$$

In the present study we have taken $r = t$. Further discussion of α is deferred to the next section.

8.05.3.4.2 The role of peeling angle Φ

Curves of the normalized peel force as a function of film thickness are shown in Figure 11 for four peel angles. The parameters characterizing the system are the same as those in Figure 6. If plasticity makes a significant contribution to the total work of fracture, then decreasing the peel angle decreases $P(1 - \cos\Phi)$ but increases the peel force P. For peel angles less than $\sim 60^\circ$, a peak in the peel force exists at an intermediate film thickness (about $t/R_0 = 6$ for the case shown). The peak is even more prominent for larger values of w_0, corresponding to less extent of reversed plastic bending.

The dependence of P/Γ_0 on the normalized interface strength $\hat{\sigma}/\sigma_Y$ is displayed in

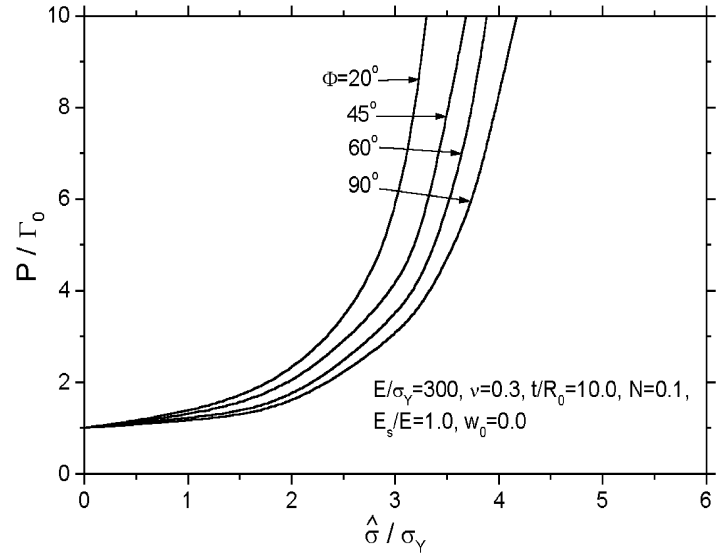

Figure 12 The normalized peel force as a function of the interface separation strength for several peel angles.

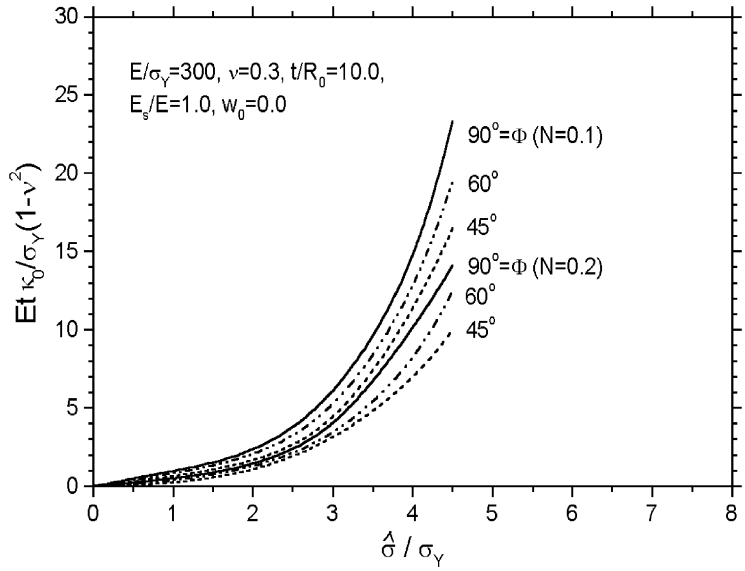

Figure 13 The normalized residual curvature as a function of the interface separation strength.

Figure 12 for four peel angles ranging from 20° to 90°. These results were computed for relatively thick films ($t/R_0 = 10$), corresponding fairly closely to the asymptote for large t/R_0. The trend with interface strength is similar to that discussed for the normal peel force. It can be seen, however, that the macroscopic work of fracture, $P(1 - \cos\Phi)$, decreases with decreasing peel angle at a given interface strength, with plasticity making less contribution. The smaller the peel angle, the larger the peel force P at a given interface strength. The residual curvature emerging from the tip region κ_0 and the opening angle α are plotted as functions of the normalized interface strength in Figures 13 and 14 for three peel angles and two levels of strain hardening, again for normalized film thickness, $t/R_0 = 10$. The trend of these quantities with interface strength is similar to that of the peel force. At low interface strength, both quantities are independent of $\hat{\sigma}$, Φ, and N. As $\hat{\sigma}/\sigma_Y$ increases, κ_0 and α increase sharply and become dependent on Φ and N.

8.05.3.4.3 The role of yield stress

The influence of the yield stress to Young's modulus ratio, σ_Y/E, on the fracture toughness in interface fracture problems of several

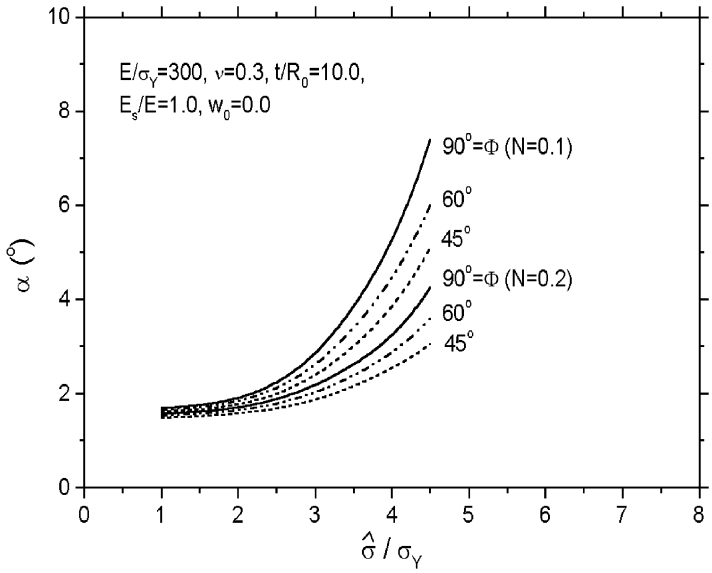

Figure 14 The crack-tip slope angle as a function of the interface separation strength.

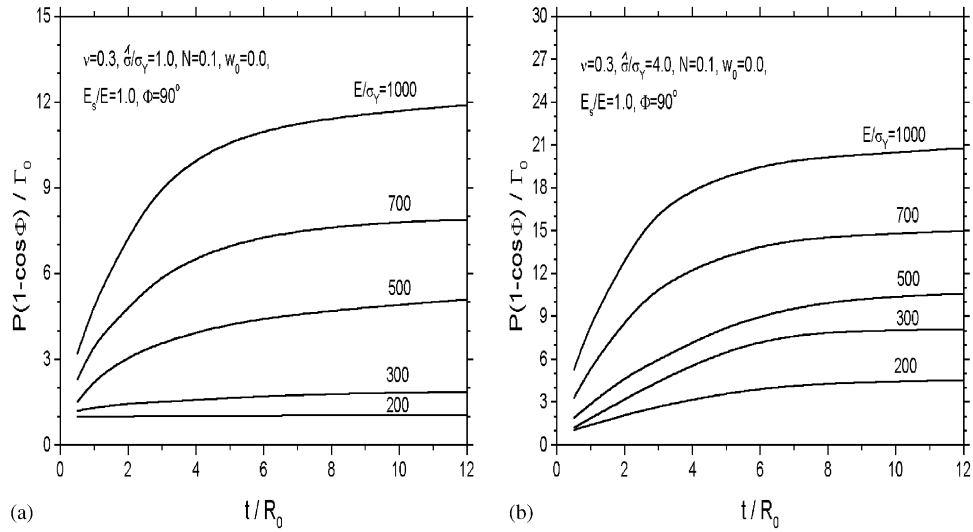

Figure 15 The normalized fracture work as a function of the film thickness and yield stress: (a) for weak interface strength, and (b) for strong interface strength.

multilayer (Tvergaard and Hutchinson, 1993) and thin film/substrate systems (Wei and Hutchinson, 1997a) has been investigated independent of the role of the yield stress in σ_Y/E and $\hat{\sigma}/\sigma_Y$. The results showed that the influence of σ_Y/E is relatively weak in those problems. However, in the present peel test problem, due to the mixed effect of the bend and near-tip constraint, interface fracture behavior is very sensitive to the ratio σ_Y/E. The peeling can be a small-scale yielding problem when the thickness is sufficiently large, in which case σ_Y/E has little effect. However, peeling involves both near-tip plasticity and "remote" plasticity and is, therefore, a large-scale yielding problem. Under these circumstances, σ_Y/E plays an important role. Figures 15(a) and (b) show how the normalized total fracture work (peel force), $P(1-\cos\Phi)/\Gamma_0$, changes with the normalized material yield stress, σ_Y/E (or yielding strain), and the thin film thickness t/R_0 for the vertical direction peeling ($\Phi = 90^\circ$). From Figure 15, it is observed that the normalized work of fracture increases dramatically with decreasing σ_Y/E. Lowering the yield stress allows the film to bend more easily thereby lowering the moment arm through which P acts, which, in turn, requires an increase in L_1. At sufficiently large values of σ_Y/E little plastic deformation

occurs and the test approaches the elastic limit. By contrast, note from Figure 15(a) that even a system with a relatively weak interface ($\hat{\sigma}/\sigma_Y = 1$) experiences significant elevation of the effective work of fracture above the elastic limit when σ_Y/E is relatively low. This is a contribution of plasticity from remote bending and not from near-tip deformation. The effect of a stronger interface can be seen in comparing Figures 5(a) and (b). As noted before, the role of the interface strength is clearly distinct from the role of the work or separation. Loosely speaking, plastic dissipation includes two parts: one from plastic bending, i.e., controlled by σ_Y/E, and the other associated with overcoming the constraint of interface adhesion to realize steady-state growth, which is primarily influenced by the yield stress through t/R_0 and $\hat{\sigma}/\sigma_Y$.

The comparisons showing the combined influence of interface strength and yield stress are extended over a very large range of t/R_0 in Figure 16. The significantly enhanced total work of peeling at intermediate thickness levels becomes evident. The prior comments about approaching the small-scale yielding limit apply here, and for the systems with weak interfaces this limit is approximately the elastic limit. Note, however, that this limit is only attained at very large t/R_0. Finally, we emphasize again that Figure 16 brings out the two distinct sources of plasticity in the peel test. In the case of weak interface in Figure 16(a), plasticity from bending has the greatest influence and at the thick film limit plastic dissipation is small with the total work of peeling approaching Γ_0. By contrast, for systems with the strong interfaces in Figure 16(b), thicker films tend to have larger total works of peeling and this is associated with the significant contribution of plastic dissipation at the crack tip in the small-scale yielding limit.

8.05.3.4.4 *Steady-state peeling of an elastic film bonded to an elastic–plastic substrate*

The GPA model and numerical solution method applies equally well to the case where the yield strength of the film is sufficiently high such that plasticity occurs only in the substrate. Here we include one example from Wei and Hutchinson (1998) to illustrate the potential of the approach. Let σ_Y denote the yield stress of the substrate and assume that Equation (8) governs substrate tensile behavior (with E replaced by E_s). The length quantity R_0 is still defined crack tip and complications arising from multiple yielding regions in the film by Equation (10), but with E replaced by E_s. Calculation of P/Γ_0 is more straightforward in this case, because the active plastic zones in the substrate is confined to the interface are absent. Curves of $P(1-\cos\Phi)/\Gamma_0$ as a function of t/R_0 are displayed for four peel angles in Figure 17 for the case where the film and substrate have identical elastic properties and the normalized interface strength is $\hat{\sigma}/\sigma_Y = 4$. When the film is elastic, the plastic zone in the substrate does not shrink to zero when t becomes small and the limiting work of fracture does not approach Γ_0. A distinct peak in the peel force occurs at $t/R_0 \cong 1$; small-scale yielding conditions are approached rapidly as t/R_0 increases. The ratio $P(1-\cos\Phi)/\Gamma_0$

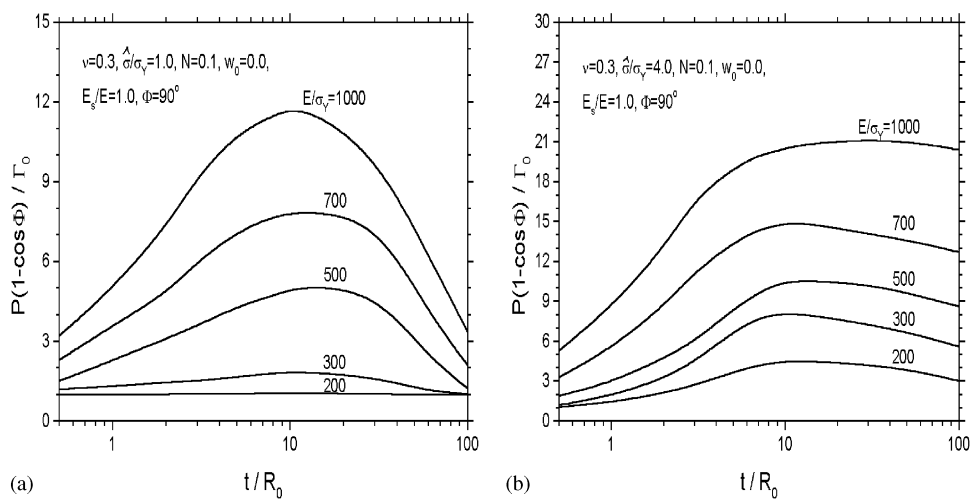

Figure 16 The normalized work of fracture work as a function of film thickness over a wide range of thickness, revealing the major effect of the yielding strain: (a) for a weak interface, and (b) for a strong interface.

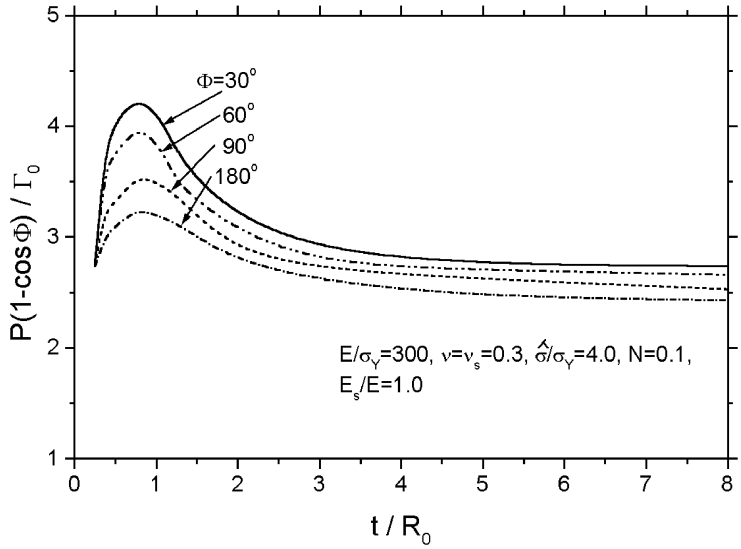

Figure 17 The normalized work of fracture work as a function of the film thickness for the case of an elastic film and an elastic–plastic substrate.

depends only weakly on the peel angle in the small-scale yielding limit implying relatively little variation in mode mixity on the peel angle.

8.05.4 PEEL TEST ANALYSIS BASED ON THE BB MODEL AND THE EPZ MODEL

8.05.4.1 Fundamental Relations

In this section, a set of results analogous to those in the last section will be presented based on the BB model endowed with an EPZ. In this way, it will be possible to make direct comparisons between the GPA model and the BB model.

As the first step in analyzing the BB model, the behavior of an elastic–plastic plate subject to a pure bending moment under plane strain conditions is presented in this subsection, as shown in Figure 18. The uniaxial stress–strain relation of the material is assumed to be the form as given in Equation (8), which can be generalized to the multiaxial stress states as

$$\bar{\sigma} = \begin{cases} (\frac{3}{2}E/(1+\nu))\bar{\varepsilon}, & \text{if } \bar{\sigma} \le \sigma_Y \\ \sigma_Y(\bar{\varepsilon}/\bar{\varepsilon}_Y)^N, & \text{if } \bar{\sigma} \ge \sigma_Y \end{cases} \tag{20}$$

Here, $\bar{\sigma} = ((3/2)\sigma'_{ij}\sigma'_{ij})^{1/2}$ and $\bar{\varepsilon} = ((2/3)\varepsilon'_{ij}\varepsilon'_{ij})^{1/2}$ are the effective stress and effective strain, with $\sigma'_{ij} = \sigma_{ij} - (1/3)\sigma_{kk}\delta_{ij}$ and $\varepsilon'_{ij} = \varepsilon_{ij} - (1/3)\varepsilon_{kk}\delta_{ij}$ as the respective deviatoric quantities, and $\bar{\varepsilon}_Y = \varepsilon_Y/[(3/2)/(1+\nu)]$.

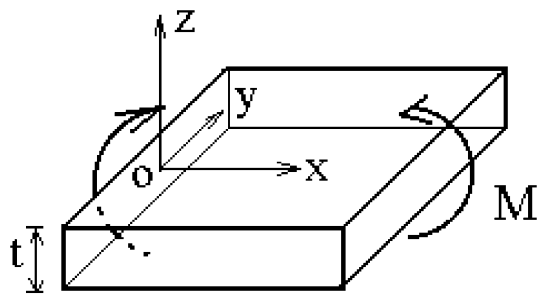

Figure 18 A beam element subject to a moment M per unit width.

8.05.4.2 Elastic Bending

For elastic bending (Figure 18), under the plane strain, the relation of bend stress and bend strain can be expressed by

$$\sigma = \frac{E}{1-\nu^2}\varepsilon = \bar{E}\varepsilon \tag{21}$$

where $\bar{E} = E/(1-\nu^2)$. At the elastic bending limit, plastic yielding occurs, $\bar{\sigma} = \sqrt{1-\nu+\nu^2}|\sigma| = \sigma_Y$, simultaneously on the top and bottom surfaces of the plate. Thus, with the usual assumption that plane sections remain planar and normal to the neutral line after loading, the axial strain at any point is a linear distribution. A relation of bending moment per unit length with beam-bending curvature is easily obtained as $M/M_0 = (2/3)\kappa/\kappa_e$, where $\kappa = d\theta/ds$ is the curvature of the middle surface at $z = 0$ with θ being the slope of the middle surface. $M_0 = (3/2)M_e$, M_e, and κ_e are elastic limit moment and

curvature, respectively, defined by

$$M_e = \frac{\sigma_Y t^2}{6\sqrt{1-\nu+\nu^2}}, \qquad \kappa_e = \frac{2(1-\nu^2)\sigma_Y}{Et\sqrt{1-\nu+\nu^2}} \quad (22)$$

Now consider the peel test geometry in Figure 2. Equilibrium at any point along the film strip requires $dM/ds = -P\sin(\Phi-\theta)$. Using $\kappa = d\theta/ds$, $M/M_0 = (2/3)\kappa/\kappa_e$ and integrating the equilibrium relation, one obtains

$$M = \sqrt{\frac{Et^3}{6(1-\nu^2)}P[1-\cos(\Phi-\theta)]} \quad (23)$$

Imposing the maximum moment condition $M_{max} = M_e$, one obtains the limit condition for elastic peeling expressed here as a condition on the film thickness:

$$t \geq t_{limit} = 18\pi(1-\nu+\nu^2)R_0\frac{P(1-\cos\Phi)}{\Gamma_0} \quad (24)$$

where the definition of R_0 is that recorded previously in Equation (10). In the elastic regime, $P(1-\cos\Phi)/\Gamma_0 = 1$. Thus, by Equation (24), elastic bending behavior will only pertain when the thickness exceeds $\sim 45\ R_0$. This estimate is generally in accord with the findings of the GPA analysis as discussed in connection with Figure 16.

8.05.4.2.1 Elastic–plastic bending

In this subsection the relation between the moment and curvature of the film is obtained prior to any unloading using a deformation theory (total strain formulation) characterization of the elastic–plastic material. The results obtained reduce to that of Kim and Aravas (1988) for the case of an elastically incompressible material.

From the elastic–plastic constitutive relations for deformation theory, when the elastic yield limit is exceeded,

$$\varepsilon_{ij}^e = \frac{1}{E}[(1+\nu)\sigma_{ij} - \nu\sigma_{kk}\delta_{ij}], \qquad \varepsilon_{ij}^p = \lambda\sigma'_{ij} = \frac{3\varepsilon^p}{2\bar{\sigma}}\sigma'_{ij} \quad (25)$$

Specifically, for the strain-hardening exponential relation in Equation (20), one has

$$\lambda = \frac{3\varepsilon^p}{2\bar{\sigma}} = \frac{(1+\nu)}{E}\left[\left(\frac{\bar{\sigma}}{\sigma_Y}\right)^{1/N-1} - 1\right] \quad (26)$$

From total strain relation $\varepsilon_{ij} = \varepsilon_{ij}^e + \varepsilon_{ij}^p$ and the plane strain condition $\varepsilon_{22} = 0$ for thin plate bend stress field, it follows that

$$\sigma_{22} = \alpha\sigma_{11} = \alpha\sigma \quad (27)$$

where

$$\alpha = \tfrac{1}{2}[1 - U_0(\bar{\sigma}/\sigma_Y)],$$
$$U_0(\bar{\sigma}/\sigma_Y) = \frac{(1-2\nu)}{1+(2/3)(1+\nu)[(\bar{\sigma}/\sigma_Y)^{1/N-1}-1]} \quad (28)$$

Thus, the effective stress and effective strain can be obtained as

$$\bar{\sigma} = \sqrt{1-\alpha+\alpha^2}|\sigma|, \qquad \bar{\varepsilon} = \frac{2\sqrt{1-\alpha+\alpha^2}}{3(1-\alpha)}|\varepsilon| \quad (29)$$

The plane bending assumption remains valid in elastic–plastic bending. Within the first elastic–plastic bending region of the peeling strip (refer to Figure 4, from point A to point B on the $M-\kappa$ curve), deformation theory can be applied. For the power-law-hardening material with $\bar{\sigma} = \sigma_Y(\bar{\varepsilon}/\bar{\varepsilon}_Y)^N$ and using (29), one can obtain the relation of bending stress to bending strain in plastic zone and consequently the moment–curvature relation:

$$M = \frac{2E\kappa\xi^3}{3(1-\nu^2)} + 2\sigma_Y^e\sqrt{1-\nu+\nu^2} \times \left(\frac{1-\nu}{\sqrt{1-\nu+\nu^2}}\frac{\kappa}{\kappa_e t/2}\right)^N \int_\xi^{t/2} \frac{1}{\sqrt{1-\alpha+\alpha^2}} \times \left(\frac{\sqrt{1-\alpha+\alpha^2}}{1-\alpha}\right)^N z^{N+1}dz$$

here $z = x_2 - (1/2)t$. The location of $z = \xi$ indicates the boundary between the elastic and plastic zones, and $\sigma_Y^e = \sigma_Y/\sqrt{1-\nu+\nu^2}$ is elastic limit bending stress. The value of the function $U_0(\bar{\sigma}/\sigma_Y)$ in Equation (28) is very small compared to unity as can be seen in Table 1 where U_0 is listed for typical $\bar{\sigma}/\sigma_Y$ and selected material parameters. Therefore, α is close to 1/2. If α is set to 1/2 with respect to small U_0, the moment–curvature relation becomes

$$M = \frac{2E\kappa\xi^3}{3(1-\nu^2)} + 2\sigma_Y^e\sqrt{1-\nu+\nu^2} \times \left(\frac{(1-\nu)}{\sqrt{1-\nu+\nu^2}}\frac{\kappa}{\kappa_e t/2}\right)^N \frac{2}{\sqrt{3}^{1-N}} \times \int_\xi^{t/2}\left[1 - NU_0 + \left(\frac{1}{2}N^2 + \frac{2}{3}N - \frac{1}{6}\right)U_0^2 + \cdots\right] \times z^{N+1}dz \quad (30)$$

The coefficients in the U_0-expansion in (30) are also small. Thus, one can neglect the influence of U_0 in this relation with the result

$$\frac{M}{M_0} = \left(\frac{2}{3} - \frac{2}{N+2^\gamma}\right)\frac{1}{(\kappa/\kappa_e)^2} + \frac{2}{N+2^\gamma}\left(\frac{\kappa}{\kappa_e}\right)^N \quad (31)$$

Table 1 Values of $U_0(\bar{\sigma}/\sigma_Y)$ at various material parameters v and N.

$\bar{\sigma}/\sigma_Y =$		1.2	1.5	2.0	2.5
$N=0.1$	$v=0.5$	0.000	0.0000	0.0000	0.0000
	$v=0.4$	0.041	0.0056	0.0004	0.0001
	$v=0.3$	0.087	0.0120	0.0009	0.0001
	$v=0.2$	0.138	0.0190	0.0015	0.0002
$N=0.2$	$v=0.5$	0.000	0.0000	0.0000	0.0000
	$v=0.4$	0.099	0.0420	0.0133	0.0055
	$v=0.3$	0.207	0.0880	0.0280	0.0120
	$v=0.2$	0.322	0.1411	0.0461	0.0191

where

$$\gamma = 2\sqrt{\tfrac{1}{3}(1-v+v^2)^{1-N}}(1-v)^N \tag{32}$$

For incompressible materials, $v=0.5$, $\gamma=1$, the result given by Kim and Aravas (1988) is recovered.

8.05.4.2.2 Elastic–plastic unloading

Elastic unloading from the state (M_0, κ_0) satisfies

$$\frac{M}{M_0} = \frac{2}{3}\frac{\kappa-\kappa_0}{\kappa_e} \tag{33}$$

It can be established that intersection point transitioning from loading to unloading (point B in Figure 4) is located at the left of crack tip for the BB model. However, the location is very near the crack tip with a distance of the order of $O(\delta_c)$. Therefore, for simplification, we take point B as the same as crack tip.

8.05.4.2.3 Summary of fundamental relations

At the unloading point (point B), $M = M_B, \kappa = \kappa_B$, from Equations (31) and (33),

$$\begin{aligned} &\frac{M_B}{M_0} = (2/3)\frac{(\kappa_B-\kappa_0)}{\kappa_e} \\ &\kappa_0 = \kappa_B + \left(\frac{3}{N+2}\gamma - 1\right)\frac{\kappa_e^3}{\kappa_B^2} - \frac{3}{N+2}\gamma\frac{\kappa_B^N}{\kappa_e^{N-1}} \end{aligned} \tag{34}$$

From the "elastica" analysis (Wei and Hutchinson, 1998),

$$\kappa_B = \sqrt{[1-\cos(\Phi-\theta_{tip})]\frac{2P}{B} + (1-w_0)\kappa_0^2} \tag{35}$$

where B is the elastic bending stiffness. In Equation (35), w_0 $(0 \le w_0 \le 1)$ characterizes the material behavior on reverse plastic loading (Bauschinger effect) as described in Section 8.05.3 and θ_{tip} is the critical value of the crack-tip slope angle. The moment–curvature relations are shown as $M/M_0 = (2/3)\kappa/\kappa_e$ for elastic bending and as Equation (31) for elastic–plastic bending, respectively.

The embedded cohesive zone will be combined with the above results. To simplify the analysis, we consider a special case of the cohesive zone model with $\lambda_1 = 0$ and $\lambda_2 = 1$ in (7), such that the distribution of the separation stress along the cohesive zone is constant and equal to $\hat{\sigma}$. Under a critical separation δ_c, the work of interface adhesion is

$$\Gamma_0 = \hat{\sigma}\delta_c \tag{36}$$

The moment equation along the cohesive zone can be derived from equilibrium as

$$M = M_B + P\sin\Phi(L-s) - \tfrac{1}{2}\hat{\sigma}(L-s)^2 \tag{37}$$

where L is length of the cohesive zone, s is the coordinate starting from the left terminal point to the right of the cohesive zone. At crack tip, $s=L$. The value of L is unknown *a priori* and will be determined as part of the solution. The rotation of beam within the cohesive zone is assumed to be small such that the curvature can be approximated as $\kappa = d\theta/ds \approx d^2w_z/ds^2$ with w_z being the deflection of middle plane of the beam. If the substrate material is taken to be rigid, the boundary conditions for the segment of the beam within the cohesive zone are

$$\begin{aligned} &w_z = 0,\ \theta = 0,\ \kappa = 0;\ \text{at } s = 0; \\ &w_z = \delta_c,\ \theta = \theta_{tip};\ \text{at } s = L \end{aligned} \tag{38}$$

Finally, we follow the procedure used in Section 8.05.3 of Wei and Hutchinson (1998) to account for reversed plastic bending without a detailed specification of the stress–strain curve under reversed stressing. This is accomplished with the aid of the parameter B_0 defined in Equation (18) and which also appeared in Equation (35).

8.05.4.3 Parametric Forms

The parametric forms governing the BB/EPZ model are essentially the same as those discussed for the model in Section 8.05.3. Under steady-state conditions, variations of peel force, residual curvature, and crack-tip slope angle will be obtained. The form of the solutions for the normalized quantities can be expressed as the functions of independent parameters according to

$$\begin{aligned}
&\frac{P(1-\cos\Phi)}{\Gamma_0} \\
&\quad = f\left(\frac{E}{\sigma_Y}, \frac{\hat{\sigma}}{\sigma_Y}, N, \nu, \frac{t}{R_0}, w_0, \Phi\right) \\
&\frac{Et\kappa_0}{\sigma_Y(1-\nu^2)} = g\left(\frac{E}{\sigma_Y}, \frac{\hat{\sigma}}{\sigma_Y}, N, \nu, \frac{t}{R_0}, w_0, \Phi\right) \\
&\theta_{tip} = r\left(\frac{E}{\sigma_Y}, \frac{\hat{\sigma}}{\sigma_Y}, N, \nu, \frac{t}{R_0}, w_0, \Phi\right)
\end{aligned} \tag{39}$$

where the length parameter R_0 is defined in Equation (10) and θ_{tip} is the crack-tip angle under steady-state peeling as determined from the BB analysis. The crack-tip angle will be compared with the analogous quantity α defined in Equation (19) for the GPA model.

As an alternative, one could take the crack tip opening displacement δ_c as the normalizing length quantity in Equation (39), because δ_c and R_0 can be related from Equations (36) and (10) as

$$R_0 = \frac{(\hat{\sigma}/\sigma_Y)(E/\sigma_Y)}{3\pi(1-\nu^2)}\delta_c \tag{40}$$

As previously emphasized, $P(1-\cos\Phi)$ in Equation (39) is also equal to the energy release rate of the peel test system under steady-state peeling with Γ_0 as the interface fracture work (or interfacial toughness) in that limit.

8.05.4.4 Results and Analyses

The normalized total fracture work (or peel force) under steady-state peeling characterizes the toughness increase due to contribution of the plastic dissipation. For pure elastic peeling, the normalized fracture work is equal to 1. The parameter κ_0 measures the residual inelastic curvature for the strip prior to reversed plastic bending, if that occurs. The crack-tip angle under the steady-state peeling in the present model is a computed quantity that relates to the parameters of the EPZ model and the film properties in a complicated way. The numerical results will be presented following the form indicated in Equation (39), and they will be compared and contrasted with the corresponding results from the GPA/EPZ model of Section 8.05.3.

Figure 19 presents the normalized fracture work $P(1-\cos\Phi)/\Gamma_0$ as a function of the film thickness, t/R_0, for a range of interface separation strengths, $\hat{\sigma}/\sigma_Y$, and for two strain hardening exponents, N. The normalized fracture work is seen to be insensitive to the interface separation strength, but somewhat sensitive to N. As t/R_0 becomes large, $P(1-\cos\Phi)/\Gamma_0$ approaches unity in accordance with the recovery of the elastic behavior. The peak values of the total work of peeling occur for $t/R_0 \approx 1$ and 2, respectively, and for $N = 0.2$ and 0.1. Figure 20 displays variations of the normalized fracture work with respect to t/R_0 for several values of N. Figure 21 illustrates the

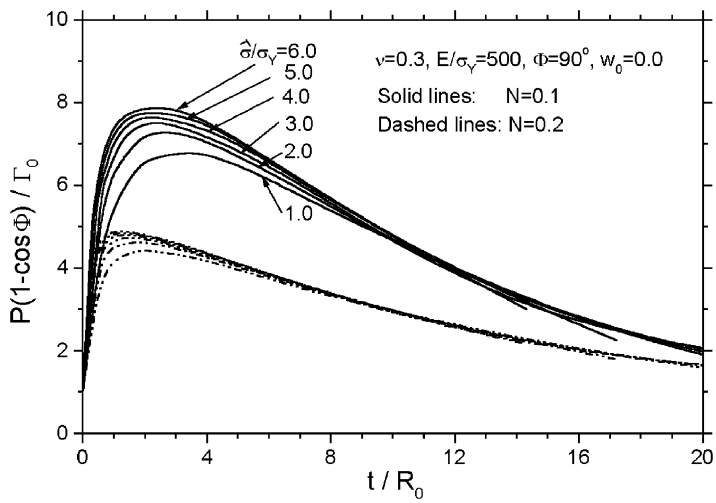

Figure 19 The normalized work of fracture as a function of the film thickness for several separation strengths.

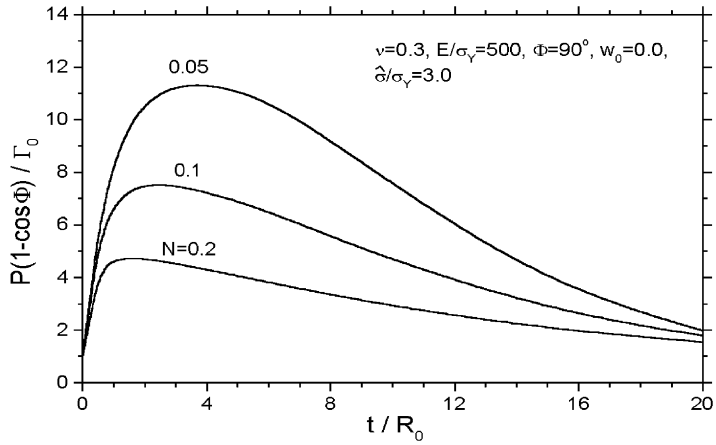

Figure 20 The normalized work of fracture as a function of the film thickness for several values of N.

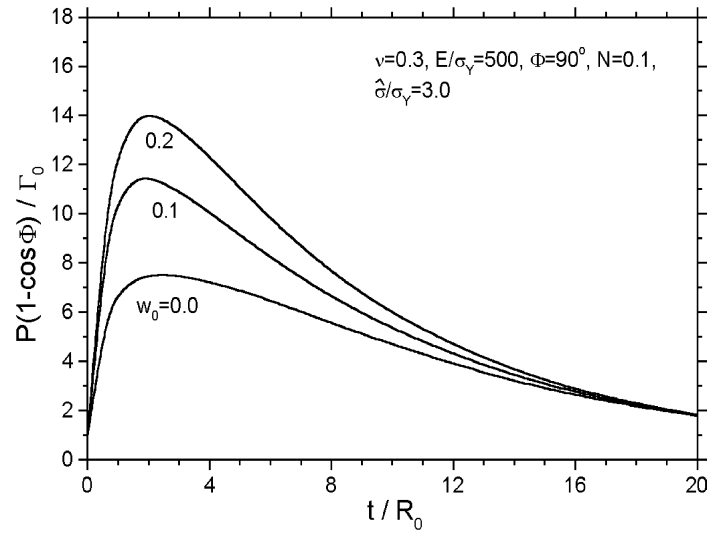

Figure 21 The normalized work of fracture work as a function of the film thickness for several values of w_0.

effect of reverse plastic bending as determined by w_0. It should be noted that realistic values of w_0 are usually much smaller than unity because the M–κ curve for thin beam bending is usually very flat (Park and Yu, 1999). For this reason relatively low values of w_0 have been assumed in Figure 21. The role of the normalized yield stress, σ_Y/E, is seen in Figure 22.

Significant differences between the BB model and the GPA model can be found when one compares the dependence on interface strength for the two models (cf. Figure 19 vs. Figures 6 and 8). Interface strength has little influence on the total work of peeling in the BB model predictions, while it is quite influential according to the GPA model if $\hat{\sigma}/\sigma_Y > 2$. It is not surprising that the BB model indicates little influence of the interface strength on the total work of fracture, because the model invokes the assumptions of beam bending even in the vicinity of the crack tip. There, the stress and strain distributions are highly nonuniform and focused, typical of those for any problem at a crack tip. The BB model cannot capture the intensely focused stresses and strains at the crack tip. This is reflected in the fact that the total work of peeling approaches Γ_0 at sufficiently large thickness for all levels of $\hat{\sigma}/\sigma_Y$. By contrast, the GPA model predicts that total work of fracture is given by the small-scale yielding work of fracture, i.e., Γ_0 plus the dissipation at the crack tip in the small-scale yielding limit. When $\hat{\sigma}/\sigma_Y > 2$, the small-scale yielding work of fracture can be many times of Γ_0. It would appear to be self-evident that the BB model should not be expected to correctly capture this important limit, and it does not. Alternatively, qualitative trends for the dependence of the total work of peeling on N, σ_Y/E, and w_0 from the BB model

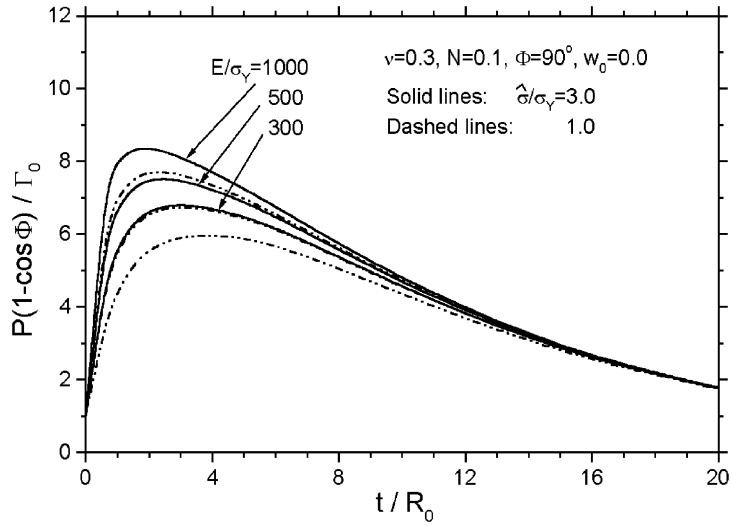

Figure 22 The normalized work of fracture as a function of the film thickness for several yield stresses.

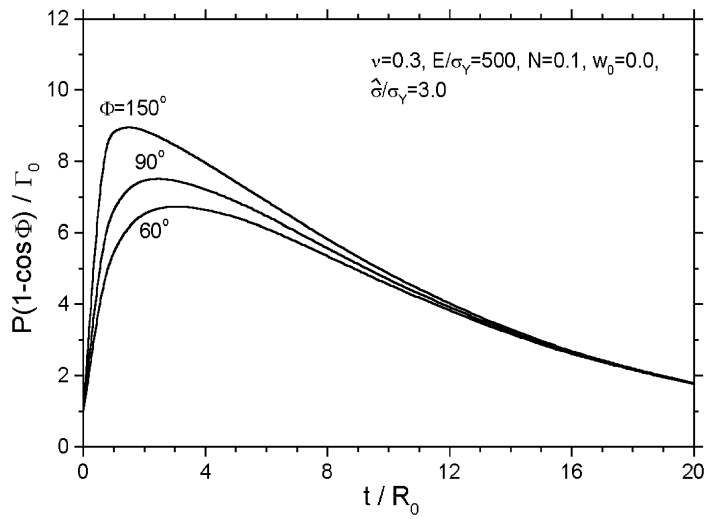

Figure 23 The normalized work of fracture as a function of the film thickness for several peel angles.

are roughly similar to those from the GPA model. Moreover, both models predict that the total work of peeling approaches Γ_0 as t/R_0 becomes small. This is the regime where plastic bending of the film is highly pronounced, but nevertheless it makes only a relatively small contribution to the total work of peeling because the film is so thin. As the film gets thinner and thinner, the plastic dissipation scales with the thickness while Γ_0 is independent of thickness.

There is another reason to question the fidelity of the BB model with the embedded cohesive zone. The computed length, L, of the cohesive zone turns out to be only of the order of the thickness of the film, t, for almost all the entire range of the parameters used in generating the results discussed above. In some instances L is less than t. Beam theory is not capable of dealing with steep variations of stresses and curvatures over distances of the order of t. The fact that the computed values of L turn out to be as short as they do strongly suggests an internal inconsistency in the combined use of the BB and EPZ models.

For completeness, several other dependencies predicted by the BB model are also presented. Figure 23 displays the influence of the peel angle Φ on the normalized fracture work. The largest effect occurs for $1 \leq t/R_0 \leq 6$. Figure 24 shows that Poisson's ratio has little effect on the total work of fracture. Thus, the modeling assumption made by Kim and Aravas (1988) that elastic compressibility can be neglected in the BB model is fully justified.

Figures 25 and 26 show the normalized residual curvature as a function of t/R_0 for the parameter combinations discussed above. As

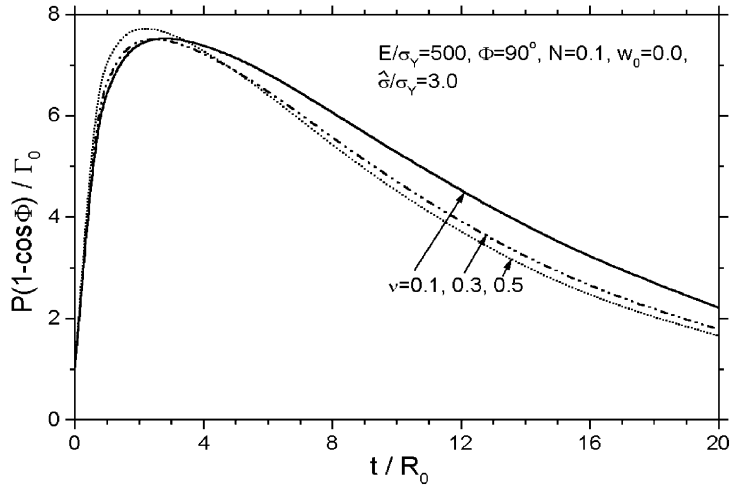

Figure 24 The normalized work of fracture as a function of the film thickness for several values of Poisson's ratio.

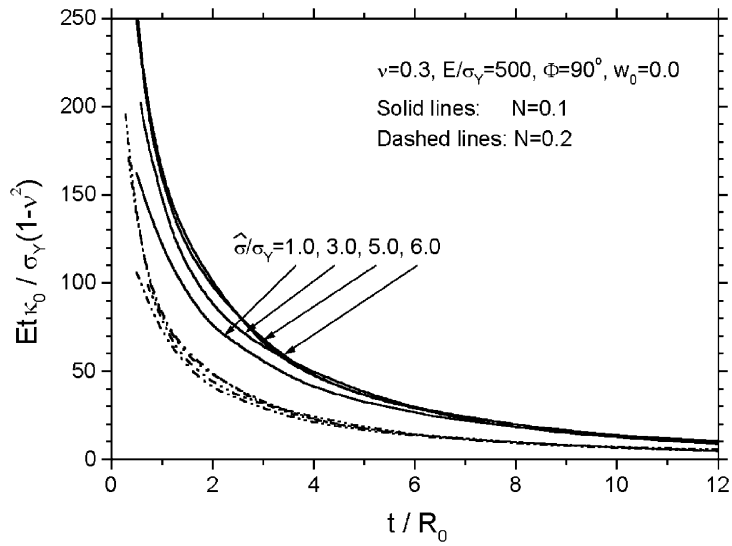

Figure 25 The normalized residual curvature as a function of the film thickness for several separation strengths.

in the case of the results presented for the GPA model, the residual curvature, κ_0, is the value emerging from the cohesive zone. It excludes any reversed plastic bending, which can be predicted with knowledge of the Bauschinger effect for the stress–strain data. As in the case of the total work of peeling, the insensitivity of the residual curvature to $\hat{\sigma}/\sigma_Y$ is unrealistic. It is interesting to note that the residual curvature from the BB model (Figures 25 and 26) is substantially higher than that predicted by the GPA model (Figures 9 and 13). This is again a consequence of the oversimplification underlying the BB model. The unidirectional stress field invoked in the bending model ignores the high constraint on plastic flow near the interface in the film in the cohesive zone. This constraint produces the high elevation of the hydrostatic stress component, which is so characteristic of any near-tip elastic–plastic field. The result is that more plastic bending occurs in the BB model in the cohesive zone than in the GPA model. It seems reasonable to assume that the GPA prediction is more trustworthy than that of the BB model. For thick films, the comparison is complicated by the fact that the BB model is unable to capture the small-scale yielding contribution to the total work of fracture.

The companion set of plots for the critical crack-tip angle, θ_{tip}, in steady-state peeling is contained in Figures 27 and 28. The strong dependence on the extrinsic thickness parameter, t/R_0, is a clear evidence that the critical

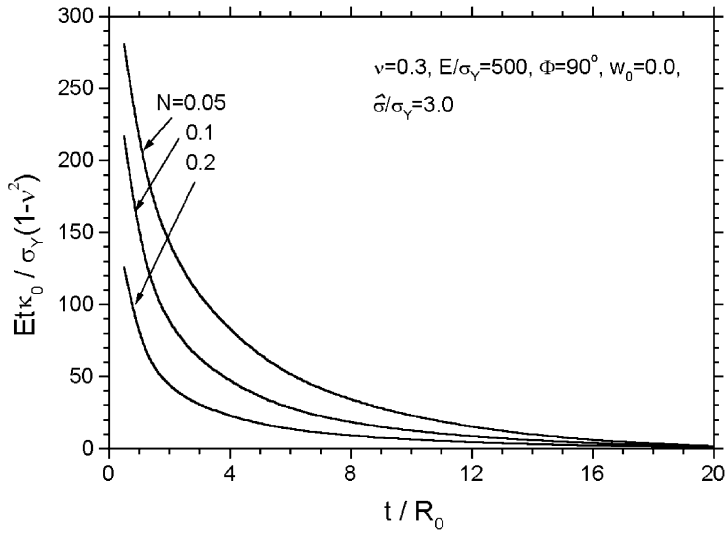

Figure 26 The normalized residual curvature as a function of the film thickness for several values of N.

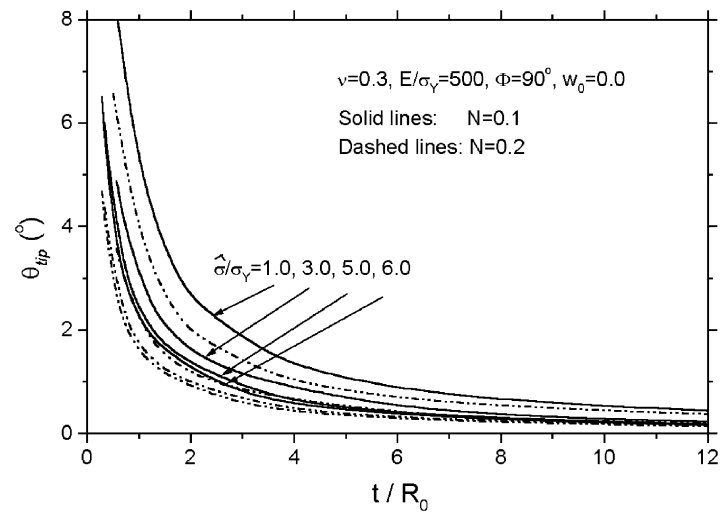

Figure 27 The crack-tip slope angle as a function of the film thickness for several values of interface separation strength.

crack tip angle cannot be viewed as a critical fracture parameter intrinsic to the interface. There is some influence of $\hat{\sigma}/\sigma_Y$ on θ_{tip}, but the trend is the opposite of that predicted by the GPA model, as seen from Figure 14. The discrepancy between two models is consistent with strong influence of $\hat{\sigma}/\sigma_Y$ on the peel force in the GPA model and the very weak dependence of the peel force on $\hat{\sigma}/\sigma_Y$ for the BB model. Further discussion of two models will be given in Section 8.05.6.

8.05.5 SPLIT TEST ANALYSIS

8.05.5.1 Preview

In the above sections, the peel test problem has been analyzed in detail. It is evident from these results that it is very difficult to determine the intrinsic interfacial toughness Γ_0 directly from the peeling experiment if significant plasticity occurs in the film (or the substrate). There are several dimensionless parameters that have substantial and complicated effects on the relation between the peel force and Γ_0. Unfortunately, the simplicity of the test in the elastic limit is lost when significant plasticity occurs.

The split test overcomes some of the difficulties associated with partitioning Γ_0 in the peel test (Wei, 2002), though it brings in the possibility of another complication. As indicated with Figure 2(b) or Figure 29, there is an additional measurable quantity, the residual curvature κ_0, which aids the partitioning process. It will be shown that this extra

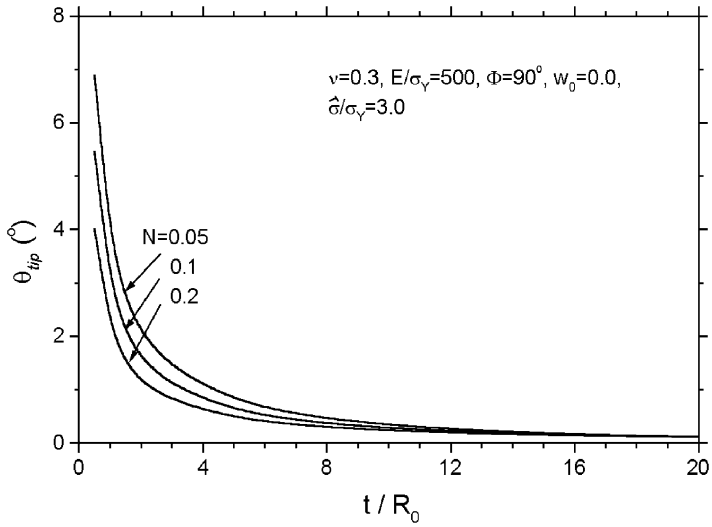

Figure 28 The crack-tip angle as a function of the film thickness for several values of N.

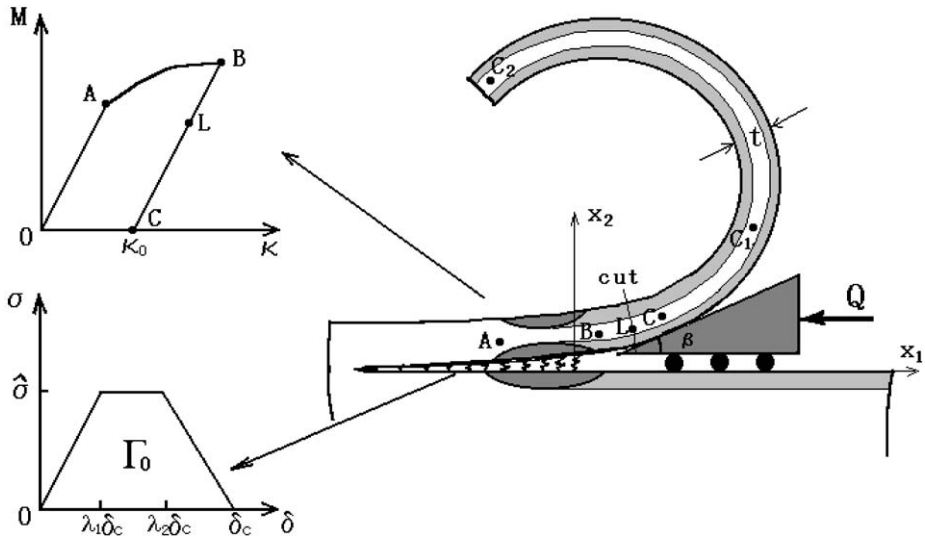

Figure 29 Split test geometry and simplified model.

quantity, with the help of the parameter relations from a beam-bending analysis, leads to the interface toughness Γ_0, provided that crack-tip dissipation is not a dominant contribution. Therefore, from this point of view, the split test has the potential as an important test method. In the present section, the split test is analyzed using both the BB model and the GPA model. Closed form parametric solutions are derived from the BB model for determining the interfacial toughness in terms of experimentally measurable quantities, all for the case in which the substrate is taken to be rigid (in Section 8.05.5.2). In the remaining parts of this section, the GPA model will be adopted. The general description for the split test problem is presented in Section 8.05.5.3. The parametric relations of the normalized split force, normalized residual curvature, and the crack-tip slope angle are computed in Section 8.05.5.4. A connection between solutions for the split test and the peel test is analyzed and discussed in Section 8.05.5.5. Finally, the general plane analysis result is applied to a wedge-loaded experiment for Al-alloy double-cantilever beam (Thouless *et al.*, 1998; Yang *et al.*, 1999) in Section 8.05.5.6. When the GPA model is used (throughout Sections 8.05.5.3–8.05.5.6), the general case is considered, in which both film and substrate are elastic–plastic. However, in order to decrease the number of parameters in our analysis, the effect of the modulus mismatch between film and substrate is neglected.

8.05.5.2 Split Test and the Interface Adhesion Toughness (BB Model)

As shown in Figure 29, the slip test involves measurement of the split force Q, the crack-tip opening slope angle θ_{tip} (see below), and the residual curvature, κ_0. Reversed bending phenomenon does not occur in the split test so that in the notation of the previous two sections, $w_0 \equiv 0$. Based on the BB model, one can obtain relations among all the govern parameters (Wei, 2002). Moreover, the analysis provides the total plastic dissipation according to

$$\begin{aligned}\Gamma^{p} = &\frac{1}{2}M_e\kappa_e - \frac{1}{2}M_B(\kappa_B - \kappa_0) \\ &+ \left(\frac{2}{3} - \frac{2}{N+2}\gamma\right)M_0\left(\kappa_e - \frac{\kappa_e^2}{\kappa_B}\right) \\ &+ \frac{2\gamma}{(N+1)(N+2)}M_0\left(\frac{\kappa_B^{N+1}}{\kappa_e^N} - \kappa_e\right)\end{aligned} \tag{41}$$

where Γ^p is the area below the M–κ curves calculated through formula in Equation (31). All parameters in the above formula are defined as the same as those in Section 8.05.4. For example, M_e and κ_e are given in (22), and γ is defined in Equation (32). In the case of split test, for the BB model, the formulas in Equations (34) and (31) are still valid, and the parametric relations in Equation (34) are rewritten as

$$\begin{aligned}&\frac{M_B}{M_0} = (2/3)\frac{(\kappa_B - \kappa_0)}{\kappa_e} \\ &\kappa_0 = \kappa_B + \left(\frac{3}{N+2}\gamma - 1\right)\frac{\kappa_e^3}{\kappa_B^2} - \frac{3}{N+2}\gamma\frac{\kappa_B^N}{\kappa_e^{N-1}}\end{aligned} \tag{42}$$

However, Equation (35) should be replaced by

$$\kappa_B = \sqrt{\frac{\sin(\beta + \theta_f - \theta_{tip})}{\sin(\beta + \theta_f)}\frac{2Q}{B} + \kappa_0^2} \tag{43}$$

Equation (43) can be derived easily, along the lines of Equation (46) given in the sequel. Here B is the bending modulus. Frictional dissipation between the splitter and the film is obtained from the force balance (Figure 29):

$$\Gamma^f = \frac{\sin\theta_f}{\sin(\beta + \theta_f)}Q \tag{44}$$

where $\theta_f = \tan^{-1} f_0$ is the frictional angle between the splitter head surface and the split film surface, and f_0 is the frictional coefficient. In the absence of friction, $\theta_f = 0$.

The interfacial toughness (work of adhesion) is obtained by

$$\Gamma_0 = Q - \Gamma^p - \Gamma^f \tag{45}$$

Utilizing Equations (41)–(45) as described in what follows, one can determine Γ_0 if split test data for κ_0, Q, and θ_{tip} are available. Given measured estimates of κ_0, Q, and θ_{tip}, one can obtain κ_B and M_B from Equation (42) and frictional angle θ_f from Equation (43), and further attain Γ^p from (41) and Γ^f from Equation (44). Finally, Γ_0 is evaluated using Equation (45). The crack-tip angle θ_{tip} is only required if nonzero friction is considered.

8.05.5.3 Characterization of the Split Test (GPA Model)

The split test geometry and related analytical model sketched in Figure 29 is now analyzed using the GPA model with an embedded fracture zone. Splitting along the interface of the film and the elastic–plastic substrate is considered. The split film thickness is t. The splitter head (usually a diamond material) is treated as a rigid material. We assume that the splitter head contacts smoothly with the split film and substrate surface such that the contact is frictionless. The splitter head contacts with the split arm at edge of the section C. The EPZ model characterizes the interfacial fracture process near the crack tip. As the crack tip steadily advances, the active plastic zones depicted by the dark shading in Figure 29 around the fracture process zone and the top surface move with the crack tip. During the fracture process, unloading zones depicted by the light shading area in Figure 29 are formed, emerging from the active plastic zones. As in the peel test analysis, the total problem is divided into two subproblems: one is a large bending for the split film, to the right of the L section, and the other is the 2D analysis for a thin film delaminating along the film/substrate interface.

8.05.5.3.1 Large bending solution for split film

The moment–curvature relation is sketched in Figure 29. As already remarked, reversed plastic bending does not occur in the split test. Upstream, a constant residual curvature with zero moment is left behind. The solution for detached part can be obtained as

$$\begin{aligned}&M = 0, \qquad \kappa = \kappa_0 \quad (\theta > \theta_c = \beta) \\ &M = B\kappa_0\left[\sqrt{1 + (2Q/B\kappa_0^2\sin\beta)\sin(\beta - \theta)} - 1\right] \\ &\kappa = \kappa_0 + M/B \quad (\theta_B < \theta \le \theta_c)\end{aligned} \tag{46}$$

where θ_B and θ_c are the slope angles with x_1-direction at the B-section and C-section, and κ_0 is the residual curvature. The formula for calculating the residual curvature κ_0 from

the plastic strains based on the second part solution has been given in Equation (17).

8.05.5.3.2 2D analysis for film delaminating under steady state

Again with reference to Figure 29, an elastic–plastic delamination of the thin film under plane strain and small deformation conditions is considered. The region includes the film to the left of the section L and the full substrate. Issues underlying the choice of the point L have been described in Section 8.05.3. The matching process for coupling the two solutions at L is similar to that described for the peel test case in Section 8.05.3.

For the split test, the total fracture work per unit width and per unit crack advance is equal to the split force Q. Neglecting the friction, one can separate the total fracture work into two parts: the interface adhesion energy Γ_0 (or interfacial toughness) and plastic dissipation Γ^{P}, the latter includes plastic bending and unloading dissipation of the separated film and the plastic dissipation due to plastic deformation and unloading in substrate. Namely

$$Q = \Gamma_0 + \Gamma^{\mathrm{p}} \tag{47}$$

For elastic splitting: $Q \equiv \Gamma_0$. Thus, in the respective elastic limits, both tests have the attractive feature that the applied force per width is the intrinsic work of fracture, assuming no frictional dissipation in the split test.

Gathering all the independent parameters and noting Figure 29, one can formally write normalized expressions for the key quantities in the test as

$$\begin{aligned} \frac{Q}{\Gamma_0} &= F_1\left(\frac{E}{\sigma_{\mathrm{Y}}}, \frac{\hat{\sigma}}{\sigma_{\mathrm{Y}}}, N, \frac{t}{R_0}, \beta, \nu\right) \\ \frac{Et\kappa_0}{\sigma_{\mathrm{Y}}(1-\nu^2)} &= F_2\left(\frac{E}{\sigma_{\mathrm{Y}}}, \frac{\hat{\sigma}}{\sigma_{\mathrm{Y}}}, N, \frac{t}{R_0}, \beta, \nu\right) \\ \alpha &= F_3\left(\frac{E}{\sigma_{\mathrm{Y}}}, \frac{\hat{\sigma}}{\sigma_{\mathrm{Y}}}, N, \frac{t}{R_0}, \beta, \nu\right) \end{aligned} \tag{48}$$

The third relation $\alpha = F_3(...)$ describes the dependence of the crack-tip angle as defined in Equation (19).

Detailed results for three functions in Equation (48) have been obtained by numerical solution of the two-part GPA model. The procedures, including the FE method, are similar to those described in Section 8.05.3.

8.05.5.4 Results and Analyses

Variations of the normalized split forces Q/Γ_0 as a function of the normalized thin layer thickness t/R_0 are shown in Figure 30 for several splitting angles. The split force Q/Γ_0 increases to an asymptote as t/R_0 increases. When t/R_0 is larger than ~ 8, the solutions become insensitive to further increases in t/R_0. The asymptote corresponds to the conventional small-scale yielding, wherein all the plasticity is confined to the immediate vicinity of the crack tip. In this limit, the plastic zone size tends to a stable value, i.e., far smaller than the split layer thickness. From Figure 30, when t/R_0 is small and decreasing, the normalized split force Q/Γ_0 decreases and tends to unity.

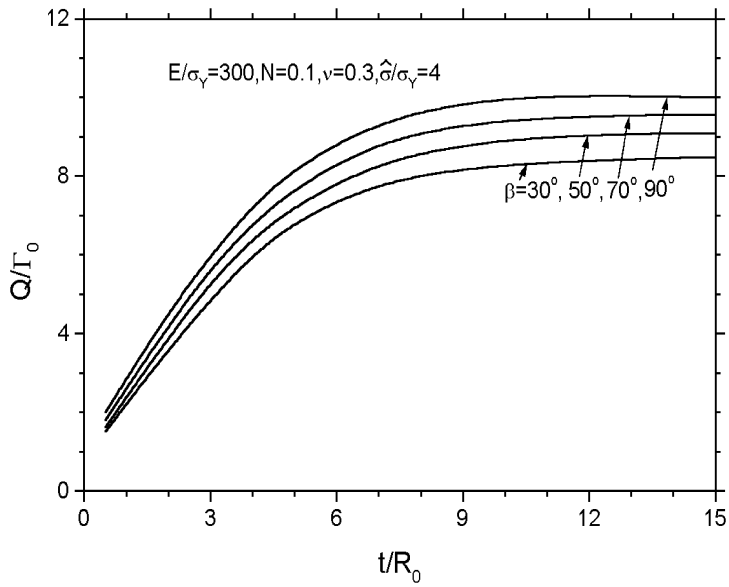

Figure 30 The variation of the normalized split force with the normalized split arm thickness for several splitter head angles.

Although in this case the plastic zone height covers the entire split layer thickness and large-scale plastic yielding occurs, the plastic dissipation contribution to the total fracture work decreases to zero as t/R_0 goes to zero, just as in the case of the peel test. Also note that increasing β can only moderately raise the value of Q/Γ_0.

Figure 31 shows the normalized residual curvature vs. the normalized layer thickness for several splitter angles. The residual curvature increases as the layer thickness decreases. Especially when t/R_0 is smaller than 3, the residual curvature increases strongly with decrease of t/R_0. However, when t/R_0 is larger than ~ 3, the residual curvature increases slowly with decreasing the split layer thickness. As in the case of the splitting force, the residual curvature is relatively insensitive to the splitting angle β, especially when t/R_0 is larger than 3.

The crack-tip angle α is plotted in Figure 32 against the normalized split layer thickness. The trends are similar to those for the residual curvature, but in this case the splitting angle β has a definite effect.

Figure 33 shows the effect of the yield stress parameter E/σ_Y on the relation of Q/Γ_0 to t/R_0. As was seen in the peel test, the effect is large. Lowering the yield stress of the film (and the substrate as well in the present calculation) significantly increases the plastic dissipation

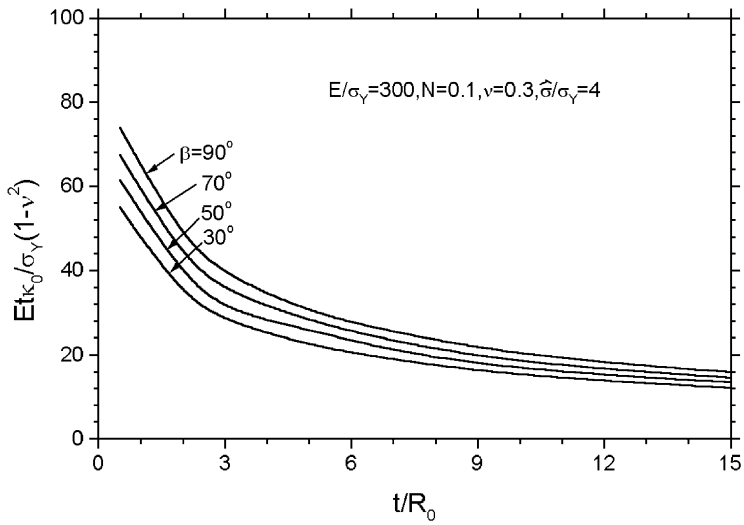

Figure 31 The variation of the normalized residual curvature with the normalized split layer thickness for several splitter head angles.

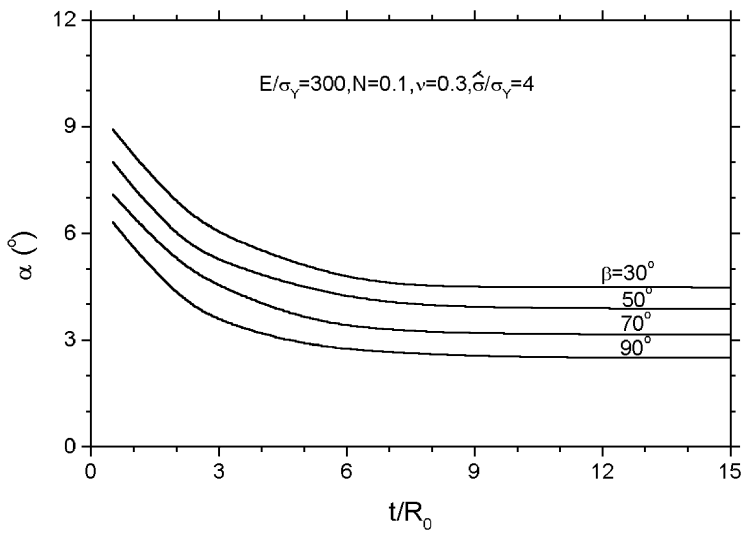

Figure 32 The variation of the crack-tip angle with the normalized split layer thickness for several splitter angles.

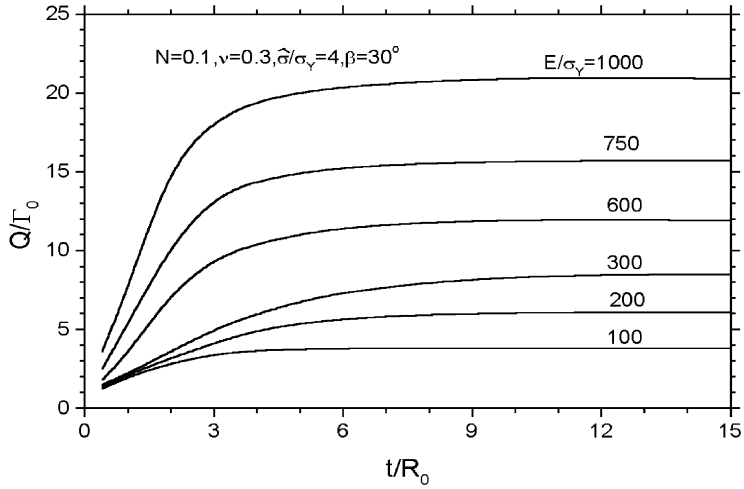

Figure 33 The relation of the normalized split force to split arm thickness for different yield strains (σ_Y/E), displaying the strong influence of the yield strain.

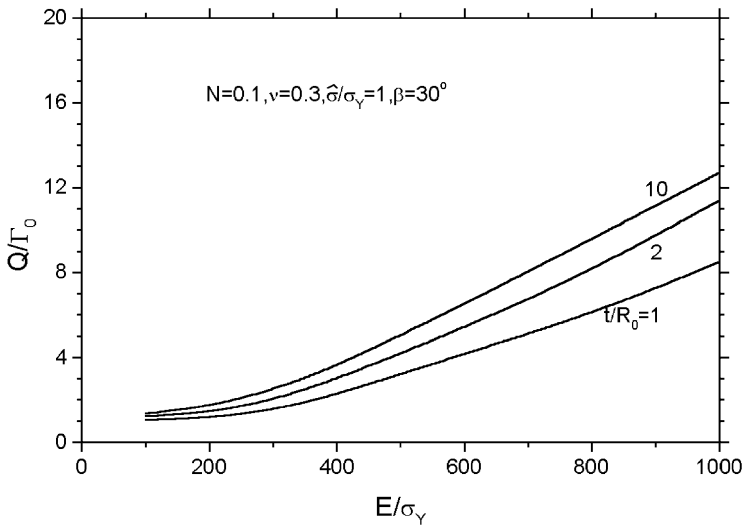

Figure 34 The effect of the material yield strain on the normalized split force for a weak separation strength.

and, therefore by Equation (47), increases Q/Γ_0.

Further investigation of the influence of the yielding strain on the total energy is shown in Figure 34 for the case of weak separation strength, $\hat{\sigma}/\sigma_Y = 1$. At $E/\sigma_Y < 300$, relatively little plastic dissipation takes place, but for larger values (lower yield strains) the plasticity contribution becomes the major portion in the total work of fracture. At the same time, the thickness of the film has only modest effect on the splitting load. The corresponding influences of E/σ_Y on the normalized residual curvature κ_0 and the crack-tip angle α are shown in Figures 35 and 36, respectively.

In Figure 37, the dependence of Q/Γ_0 on the normalized separation strength $\hat{\sigma}/\sigma_Y$ and the material strain-hardening exponent N is displayed for $E/\sigma_Y = 300$. The trends are qualitatively similar to the corresponding results for the peel test. For $E/\sigma_Y = 300$, plastic dissipation plays a small role as long as $\hat{\sigma}/\sigma_Y < 2$, but it becomes increasingly important as the interface strength increases due to the higher force required to separate the film. Materials with low strain hardening become very difficult to split from the substrate when $\hat{\sigma}/\sigma_Y > 3$. This effect is similar to that observed for small-scale yielding fracture toughness for homogeneous materials or for interfaces as shown in earlier studies (Wei and Hutchinson, 1997a, 1998; Tvergaard and Hutchinson, 1992, 1993; Evans *et al.*, 1999). To some extent it also reflects limitations of the conventional plasticity used in the present modeling, as will be discussed in the conclusions.

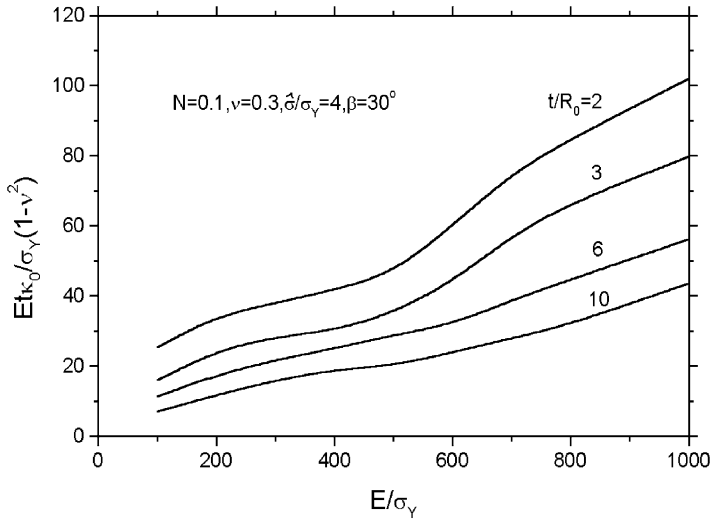

Figure 35 The effect of the yielding strain on the normalized residual curvature for several split layer thicknesses.

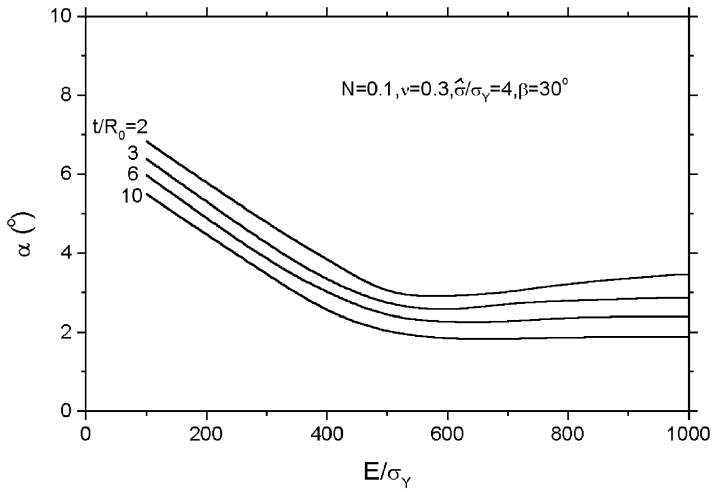

Figure 36 The effect of the yielding strain on the crack-tip angle for several split layer thicknesses.

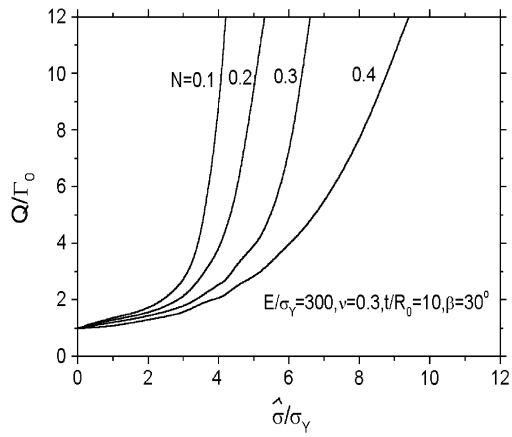

Figure 37 The influences of the normalized separation strength on the normalized split force for different strain hardening exponent values N.

8.05.5.5 Connection between Split Test and Peel Test

Let us start with the peel test, and consider a peel angle Φ larger than $\pi/2$. Let $\Phi = \pi/2 + \beta$ and note the definitions of the respective angles in Figures 29 and 38. As motivated by the sketch in Figure 38, we will compare the peel test at a peel angle $\Phi = \pi/2 + \beta$ with the split test for a splitter of angle β. The total work of separation in the peel test is $P(1 + \sin\beta)$, while that in the split test is Q. A correspondence between the solutions for the two tests is made by requiring the total work of separation to be the same in each test, i.e., $Q = P(1 + \sin\beta)$. The GPA model will be applied to both tests with the respective bending solutions and FEM results matched at the common point L. With

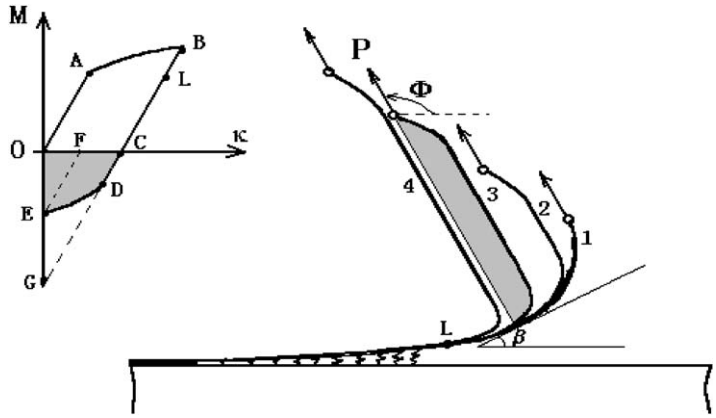

Figure 38 The peel test geometry and analytical models. The shaded area indicates reversed bending. Case 1 has no reversed bending. From case 1 to case 4, the reversed bending strength w_0 increases. The peel angle $\Phi = 90^\circ + \beta$ is larger than 90°.

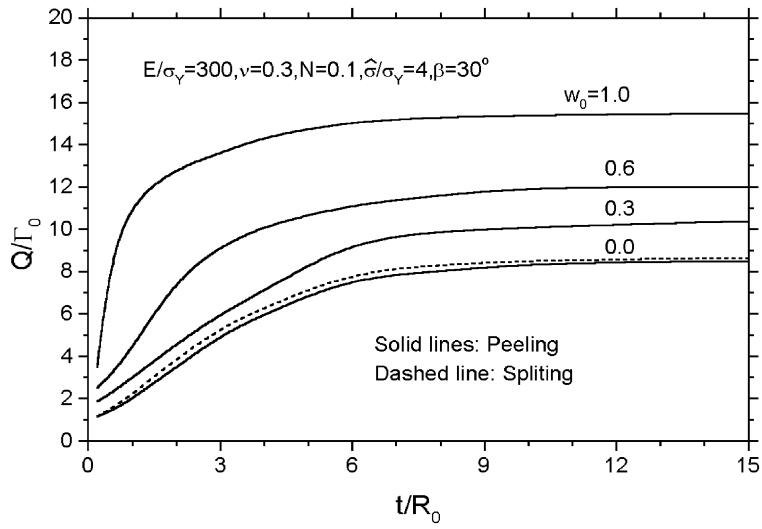

Figure 39 The variation of the normalized energy rate with the normalized peeled layer thickness for several w_0 values of the peel test problem. The dashed line corresponds to the split test result.

this construction, the portion of the problem analyzed by FEM is the same in each of the two tests.

From Equation (18), the bending solution of the peel test is

$$M = B\kappa_0 \left\{ \sqrt{\begin{array}{l} 1 + [2Q/B\kappa_0^2(1+\sin\beta)] \\ \times[1+\sin(\beta-\theta)] - w_0 \end{array}} - 1 \right\} \tag{49}$$

$$\kappa = \kappa_0 + M/B(\theta_B < \theta < \Phi = \pi/2 + \beta)$$

The formula for computing κ_0 is the same as in Equation (17). Unlike the split test, κ_0 in the peel test is difficult to measure since the peeled arm undergoes a very complicated deformation due to reversed plastic bending. The parameter w_0 is that introduced in Section 8.05.3 (Figure 38); it has the range $0 \le w_0 \le 1$. The corresponding beam solution for the split test is given by Equation (46). Note that the inclination angle at the section L, $\theta = \theta_L$, is much smaller than β. When $w_0 = 0$, the difference between the solutions from Equations (49) and (46) at L comes from the two terms: $(1+\sin(\beta-\theta_L))/(1+\sin\beta)$ and $\sin(\beta-\theta_L)/\sin\beta$. The difference between these solutions is very small since $\theta_L \ll \beta$. It is this observation that justifies the present construction of the correspondence between the two tests. The correspondence is less good for large w_0 in the peel test, as seen in Figure 39 for one particular numerical example. The major conclusion to be drawn is that in the hypothetical absence of reversed bending in the peel test, the two tests are expected to give similar total works of fracture if the peel and splitting angle satisfy $\Phi = \pi/2 + \beta$.

8.05.5.6 Application to a Wedge-loaded Experiment for Al-alloy Double-cantilever Beam

Thouless and co-workers have carried out a series of wedge-loaded experiments for the Al-alloy double-cantilever beam specimens (Thouless *et al.*, 1997, 1998; Yang *et al.*, 1999). They employed a nominally rigid wedge with a rounded tip. The wedge test differs only slightly from the split test. By moving the wedge towards the crack tip at the split, a pair of driving forces is exerted on the each split arm and makes the double-cantilever beam delaminate along the bonded interface. The contact points move forward with crack tip. The influence of the curvature radius of wedge tip on the residual radius of the split arm was obtained. The closer the contact point between wedge and split arm to the crack tip, the smaller the radius of curvature of the wedge tip. Similarly, for the sharp wedge (splitter head) as discussed here, as the splitter angle β decreases, the contact point between splitter face and split arm is close to crack tip. Therefore, the splitter angle β for a sharp wedge plays a similar role as the curvature radius of a blunt wedge. We apply the split test analysis in last subsection to the test geometry of a symmetrical double-cantilever beam. For a double-cantilever beam specimen in a wedge-loaded split test, β is the half tip angle of the wedge. For the purpose of comparison, we will consider the same test geometry and Al-alloy material used in the experiments by Thouless and co-workers. By comparing the present analysis with their experimental results, a connection between the curvature radius of the blunt wedge and the splitter angle of the sharp wedge will be established.

For the material Al alloy considered in Yang *et al.* (1999), the material is characterized by a yielding stress of $\sigma_Y \approx 100\,\text{MPa}$, a Young's modulus of 70 GPa, and a Poisson's ratio of 0.3. Therefore, $(E/\sigma_Y, \nu) = (700, 0.3)$ in the present analysis. For the moderate hardening metal, the value $N = 0.2$ is adopted for the stress–strain relations in Equation (8). For weakly bonded double-cantilever beam specimen, corresponding to a relatively large fracture process zone, Yang *et al.* (1999) measured $\Gamma_0 = 1.4\,\text{kJ m}^{-2}$ and $\hat{\sigma}/\sigma_Y = 1$. From Equation (10), the plastic zone size in small-scale yielding case is computed as $R_0 = 1.15\,\text{mm}$.

The symmetry of the double-cantilever beam specimen enables only one wing of the double-cantilever beam to be considered. On the interface (symmetry surface), the mode I crack condition pertains. The problem geometry becomes the same as Figure 29, assuming that the plastic dissipation from the film is much larger than that from the substrate, i.e., as long as the substrate is taken as a rigid material in there. The correspondence between the two models is not exact because the displacement tangential to the interface is constrained to be zero in the split test but not in the wedge test. However, this difference is not expected to be important. The driving force Q in Figure 29, the critical crack-tip opening displacement, and the corresponding interface fracture toughness Γ_0 in a split test are only half of their counterparts in the double-cantilever test. However, the ratio Q/Γ_0 is unchanged, equal to the corresponding ratio of the double-cantilever beam case.

Figure 40 shows the normalized residual curvature as a function of the splitter angle for various film thicknesses. The normalized

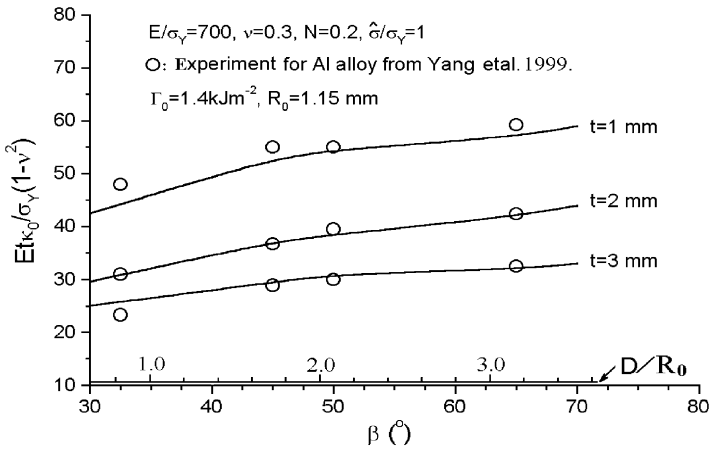

Figure 40 Normalized residual curvature as a function of splitter shape: sharp wedge with angle β (solid lines) and blunt wedge with tip curvature diameter D (source: circles; experiments for Al alloy from Yang *et al.* (1999)).

residual curvature slowly increases with increasing β. However, the residual curvature increases markedly as the film thickness varies. The experimental results of Yang *et al.* (1999) are also shown in Figure 40, plotted against the normalized wedge tip diameter D/R_0 rather than β. The analytical results are surprisingly consistent with the experimental results within realistic domains of geometrical parameters, β and D/R_0. In Figure 40, $1/\kappa_0$ is the residual radius of curvature of the split film. In this analysis, $E/\sigma_Y(1-\nu^2) = 769$, and, in Figure 40 at $\beta = 50^\circ$, the residual radii are about 14 mm, 40 mm, and 77 mm, respectively, for split film thickness $t = 1$ mm, 2 mm, and 3 mm. Figure 40 establishes a strong correspondence between the sharp wedge parameter β and the blunt wedge parameter D. From the figure, $D = 1$ mm of blunt wedge case corresponds to $\beta = 32.5^\circ$ of sharp wedge case, and $D = 3.6$ mm corresponds to $\beta = 65^\circ$.

In the application, the split force Q (driving force per unit width) is also obtained. For example, at $\beta = 50^\circ$ the split forces (per unit width) are $4.4\,\mathrm{N\,mm^{-1}}$, $5.8\,\mathrm{N\,mm^{-1}}$, and $6.9\,\mathrm{N\,mm^{-1}}$, respectively, for split film thickness $t = 1$ mm, 2 mm, and 3 mm.

8.05.6 CONCLUDING REMARKS ON MODELING THE PEEL TEST

For what is regarded generally as a simple test, the peel test is remarkably complicated when plastic deformation makes a significant contribution to the total peel work of fracture. Aside from its apparent simplicity and popularity, the peel test does not provide an easy means of determining the interface adhesion energy Γ_0, except under conditions where plastic dissipation is negligible. It should be apparent from this chapter that modeling the peel test with the objective of partitioning the total work of peel to obtain Γ_0 is far from straightforward. The cohesive zone model combined with the detailed continuum analysis near the crack tip (the GPA/EPZ model) brings out the combined roles of the two parameters characterizing the interface Γ_0 and interface strength $\hat{\sigma}$, in determining the peel force and the contribution of plastic dissipation to the total work of fracture. The coupling between these parameters is highly nonlinear. The GPA/EPZ model reveals a fairly clear qualitative picture of the two major sources of the plastic dissipation: localized crack-tip plasticity, Γ_p^{tip}, and "large-scale plasticity" due to bending, $\Gamma_p^{bending}$. Figure 41 presents a schematic overview of the regimes of these contributions to the total work of fracture. At high interface strength, as measured by $\hat{\sigma}/\sigma_Y$, local crack-tip plastic dissipation can constitute a large fraction of the total work of fracture, such that the peel force is many times of Γ_0, as indicated by regions B and C in Figure 41. When t/R_0 becomes sufficiently large, plasticity in bending does not occur and Γ_p^{tip} becomes the major source of the dissipation (C). However, as t/R_0 decreases, bending plasticity also comes into play. When the interface strength is small and t/R_0 is large, in region D, the entire peeling process is elastic and the test provides a direct evaluation of Γ_0. However, even a system with a relatively weak

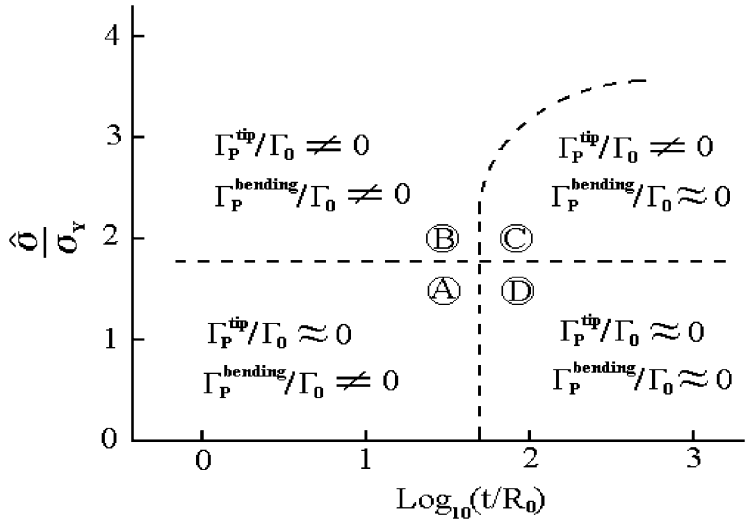

Figure 41 A schematic displaying the regimes of plastic dissipation in the peel test as dependent on the normalized interface strength and the normalized film thickness. The plot is roughly applicable for $\sigma_Y/E > 1/500$. The boundary between regions A and B is quite sensitive to σ_Y/E.

interface will produce $\Gamma_p^{bending}$ at small t/R_0 as in region A of Figure 41. But as discussed in Section 8.05.3, the ratio $\Gamma_p^{bending}/\Gamma_0$ may, nevertheless, be small if the volume of material (i.e., thickness of the film) is sufficiently small. The location of boundaries between different regimes in Figure 41 depends on another parameter, σ_Y/E, and to a lesser, but nevertheless significant, extent on the strain-hardening index, N.

In principle, the GPA/EPZ model provides a computational means of partitioning the total work of fracture into the interface adhesion energy and plastic dissipation. However, there are two primary difficulties in using such a model to determine the interface adhesion energy Γ_0 from peel test data. The first is simply the fact that at least three dimensionless parameters play important roles in the theoretical results: $\hat{\sigma}/\sigma_Y$, σ_Y/E, and t/R_0. One of these, $\hat{\sigma}/\sigma_Y$, cannot be determined directly and is therefore difficult to assign. These are no issues that impede the usefulness of the model for qualitative understanding, but they make it difficult to obtain a reliable quantification for specific peel systems.

The second difficulty relates to the inadequacy of conventional plasticity theory used in carrying out the calculations (e.g., the J_2 flow theory). For metals, there are compelling reasons to believe that conventional plasticity theory significantly underestimates hardening and stresses when the gradients of plastic strain are large as, e.g., at a crack tip (Fleck and Hutchinson, 1997). More and more experimental evidence is accruing indicating that, when nonuniform deformation occurs on the μm scale, elevations in stresses occur that are several times those observed at larger scales at equivalent strain levels (Bagchi *et al.*, 1994; Bagchi and Evans, 1996; Lipkin *et al.*, 1998; Evans *et al.*, 1999). Stress elevation fosters interface separation at the tip of a crack on a strong interface. Size effects resulting in stress elevation at small scales have been found in the other kinds of problems as well, such as microindentation tests (Stelmashenko *et al.*, 1993; Ma and Clarke, 1995; McElhaney *et al.*, 1998; Wei *et al.*, 2001), torsion tests of thin copper wires (Fleck *et al.*, 1994), as well as bending tests of thin films (Stolken and Evans, 1998). Plasticity theories have been formulated that incorporate a material length scale and size effects (e.g., Fleck and Hutchinson, 1993, 1997; Aifantis, 1992; Acharya and Bassani, 1996; Gao *et al.*, 1999; Huang *et al.*, 2000), but at this stage of their development it is probably to soon to be able to use them for quantitative modeling. Qualitative trends expected from a GPA/EPZ model, which employs the enhanced μm scale plasticity theory, can be seen in Wei and Hutchinson (1997b).

Finally, based on the findings in Section 8.05.4, it has to be stated that a model based on beam (or plate) theory coupled with a cohesive zone does not seem to be viable. As has been emphasized in Section 8.05.4, such a model fails to capture near-tip plastic dissipation and therefore is unable to give realistic predictions, or even correct trends, for relatively thick films with strong interfaces. The very important role of interface strength is not revealed at all by this type of model. It should be no surprise that this class of model is unable to capture near-tip behavior, since beam theory is derived under the tacit assumption that variations along the beam take place over lengths that are long compared to the beam thickness. Near-tip plasticity occurs on the scale of the thickness or even smaller. Even more troubling, the length of the cohesive zone as computed from this class of models turns out to be of the order of the thickness in nearly all cases. This is a clear signal that the modeling assumptions are inconsistent with the use of beam theory. While these statements clearly imply that coupling a beam model to a cohesive zone does not make sense, it does not constitute an argument against the usefulness of other models based on beam theory. Models that employ the crack-tip opening angle as computed from a beam model (without a cohesive zone) may be useful if the critical opening angle is treated as a characterizing parameter. However, the basic goal of partitioning the intrinsic work of fracture in the test is not achieved with a model of this type.

ACKNOWLEDGMENTS

The work of Y. Wei was supported by the National Natural Science Foundations of China through Grants 19891180 and 19925211, and jointly supported by Chinese Academy of Sciences through ''Bai Ren Plan'' and Division of Engineering and Applied Sciences, Harvard University. The work of J. W. Hutchinson was supported by the US National Science Foundation through grant CMS-96-34632.

8.05.6 REFERENCES

A. Acharya and J. L. Bassani, 1996, On non-local flow theories that preserve the classical structure of incremental boundary value problems. In: ''Micromechanics of Plasticity and Damage in Multiphase Materials, IUTAM Symposium,'' eds. A. Pineau and A. Zaou, Kluwer Academic, Paris, pp. 3–10.

E. C. Aifantis, 1992, On the role of gradients in the localization of deformation and fracture. *Int. J. Eng. Sci.*, **30**, 1279–1299.

H. Asai, N. Iwase and T. Suga, 2001, Influence of ceramic surface treatment on peel-off strength between aluminum nitride and epoxy-modified polyaminobismaleimide adhesive. *IEEE Trans. Adv. Packaging*, **24**, 104–112.

A. S. Argon, V. Gupta, H. S. Landis and J. A. Cornie, 1989, Intrinsic toughness of interfaces between SiC coatings and substrates of Si or C fibre. *J. Mater. Sci.*, **24**, 1207–1218.

A. G. Atkins and Y. W. Mai, 1986, Residual strain energy in elastoplastic adhesive and cohesive fracture. *Int. J. Fract.*, **30**, 203–221.

A. Bagchi and A. G. Evans, 1996, The mechanics and physics of thin film decohesion and its measurement. *Interf. Sci.*, **3**, 169–193.

A. Bagchi, G. E. Lucas, Z. Suo and A. G. Evans, 1994, A new procedure for measuring the decohesion energy for thin ductile films on substrates. *J. Mater. Res.*, **9**, 1734–1741.

G. E. Beltz, J. R. Rice, C. F. Shih and L. Xia, 1996, A self-consistent model for cleavage in the presence of plastic flow. *Acta Mater.*, **44**, 3943–3954.

J. J. Bickerman, 1957, Theory of peeling through a hookean solid. *J. Appl. Phys.*, **28**, 1484–1485.

D. A. Bigwood and A. D. Crocombe, 1989, Elastic analysis and engineering design formulae for bonded joints. *Int. J. Adhes. Adhes.*, **9**, 229–242.

K. Bundy, U. Schlegel, B. Rahn, V. Geret and S. Perren, 2000, Improved peel test method for measurement of adhesion to biomaterials. *J. Mater. Sci. (Mater. Med.)*, **11**, 517–521.

M. D. Chang, K. L. DeVries and M. L. Williams, 1972, The effects of plasticity in adhesive fracture. *J. Adhes.*, **4**, 221–231.

W. T. Chen and T. F. Falvin, 1972, Mechanics of film adhesion: elastic and elastic–plastic behavior. *IBM J. Res. Dev.*, **16**, 203–213.

J. W. Choi and T. S. Oh, 2001, Peel strength and peel angle measured by the T-peel test on Cr/BPDA-PDA interfaces. *J. Adhes. Sci. Tech.*, **15**, 139–152.

A. D. Crocombe and R. D. Adams, 1981, Peel analysis using the finite element method. *J. Adhes.*, **12**, 127–139.

A. D. Crocombe and R. D. Adams, 1982, An elasto-plastic investigation of the peel test. *J. Adhes.*, **13**, 241–267.

R. H. Dean and J. W. Hutchinson, 1980, Quasi-static steady crack growth in small scale yielding. In: "Fracture Mechanics, ASTM STP 700," ed. American Society for Testing Materials, Philadelphia, pp. 383–405.

A. G. Evans, M. D. Drory and M. S. Hu, 1988, The cracking and decohesion of thin films. *J. Mater. Res.*, **3**, 1043–1049.

A. G. Evans, J. W. Hutchinson and Y. Wei, 1999, Interface adhesion: effects of plasticity and segregation. *Acta Mater.*, **47**, 4093–4113.

R. Feliu-Baez, H. E. Lockhart and G. Burgess, 2001, Correlation of peel and burst tests for pouches. *Packaging Tech. Sci.*, **14**, 63–69.

N. A. Fleck and J. W. Hutchinson, 1993, A phenomenological theory for strain gradient effects in plasticity. *J. Mech. Phys. Solids*, **41**, 1825–1857.

N. A. Fleck and J. W. Hutchinson, 1997, Strain gradient plasticity. In: "Advances in Applied Mechanics," eds. J. W. Hutchinson and T. Y. Wu, Academic Press, New York, vol. 33, pp. 295–361.

N. A. Fleck, G. M. Muller, M. F. Ashby and J. W. Hutchinson, 1994, Strain gradient plasticity: theory and experiments. *Acta Metall. Mater.*, **42**, 475–487.

H. Gao, Y. Huang, W. D. Nix and J. W. Hutchinson, 1999, Mechanism-based strain gradient plasticity: I Theory. *J. Mech. Phys. Solids*, **47**, 1239–1263.

J. L. Gardon, 1963, Peel adhesion: II. A theory analysis. *J. Appl. Polym. Sci.*, **7**, 643–664.

A. N. Gent and G. R. Hamed, 1975, Peel mechanics. *J. Adhes.*, **7**, 91–95.

A. N. Gent and G. R. Hamed, 1977, Peel mechanics for an elastic–plastic adherend. *J. Appl. Polym. Sci.*, **21**, 2817–2831.

Y. Huang, H. Gao, W. D. Nix and J. W. Hutchinson, 2000, Mechanism-based strain gradient plasticity: II. Analysis. *J. Mech. Phys. Solids*, **48**, 99–128.

A. B. Hulcher, J. M. Marchello and J. A. Hinkley, 1999, Wedge peel testing for automated fiber placement. *J. Adv. Mater.*, **13**, 37–42.

J. W. Hutchinson, 1974, "On Steady Quasi-static Crack Growth," Harvard University report, DEAP S-8 (AFSOR-TR-74-1042).

J. W. Hutchinson and Z. Suo, 1992, Mixed mode cracking in layered materials. In: "Advances in Applied Mechanics," eds. J. W. Hutchinson and T. Y. Wu, Academic Press, New York, pp. 63–191.

T. Igarashi, 1984, Peel strength and energy dissipation. In: "Adhesive Joints: Formulation, Characteristics and Testing," ed. K. L. Mittal, Plenum, New York, pp. 419–432.

C. Jouwersma, 1960, On the theory of peeling. *J. Polym. Sci.*, **45**, 253–255.

D. H. Kaeble, 1959, Theory and analysis of peel adhesions: mechanisms and mechanics. *Trans. Soc. Rheol.*, **3**, 161.

D. H. Kaeble, 1960, Theory and analysis of peel adhesions: bond stresses and distributions. *Trans. Soc. Rheol.*, **4**, 45–73.

M. Kawabe, S. Tasaka and N. Inagaki, 2000, Effects of surface modification by oxygen plasma on peel adhesion of pressure-sensitive adhesive tapes. *J. Appl. Polym. Sci.*, **78**, 1392–1401.

K. Kendall, 1973, The shapes of peeling solid films. *J. Adhes.*, **5**, 105–117.

J. Kim, K. S. Kim and Y. H. Kim, 1989, Mechanical effects in peel adhesion test. *J. Adhes. Sci. Technol.*, **3**, 175–187.

K. S. Kim and N. Aravas, 1988, Elastoplastic analysis of the peel test. *Int. J. Solids Struct.*, **24**, 417–435.

K. S. Kim and J. Kim, 1988, Elasto-plastic analysis of the peel test for thin film adhesion. *J. Eng. Mater. Technol.*, **110**, 266–273.

A. J. Kinloch, 1987, "Adhesion and Adhesives: Science and Technology," Chapman and Hall, New York.

A. J. Kinloch, C. C. Lau and J. G. Williams, 1994, The peeling of flexible laminates. *Int. J. Fract.*, **66**, 45–70.

D. M. Lipkin, D. R. Clarke and A. G. Evans, 1998, Effect of interfacial carbon on adhesion and toughness of gold–sapphire interfaces. *Acta Mater.*, **46**, 4835–4850.

Q. Ma and D. R. Clarke, 1995, Size dependent hardness of silver single crystals. *J. Mater. Res.*, **10**, 853–863.

K. W. McElhaney, J. J. Vlassak and W. D. Nix, 1998, Determination of indenter tip geometry and indentation contact area for depth-sensing indentation experiments. *J. Mater. Res.*, **13**, 1300–1306.

A. K. Moidu, A. N. Sinclair and J. K. Spelt, 1995, Analysis of the peel test: prediction of adherend plastic dissipation and extraction of fracture energy in metal-to-metal adhesive joints. *J. Test. Eval.*, **23**, 241–253.

A. K. Moidu, A. N. Sinclair and J. K. Spelt, 1998, On the determination of fracture energy using the peel test. *J. Test. Eval.*, **26**, 247–254.

A. Needleman, 1987, A continuum model for void nucleation by inclusion debonding. *J. Appl. Mech.*, **54**, 525–531.

D. W. Nicholoson, 1977, Peel mechanics with large bending. *Int. J. Fract.*, **13**, 279–287.

I. S. Park and J. Yu, 1998, An X-ray study on the mechanical effects of the peel test in a Cu/Cr/polyimide system. *Acta Mater.*, **46**, 2947–2953.

Y. B. Park, I. S. Park and J. Yu, 1999, Interfacial fracture energy measurements in the Cu/Cr/polyimide system. *Mater. Sci. Eng. A*, **266**, 261–266.

Y. B. Park and J. Yu, 1999, Phase angle in the Cu/polyimide/alumina system. *Mater. Sci. Eng. A*, **266**, 109–114.

D. M. Parks, P. S. Lam and R. M. McMeeking, 1981, Some effects of inelastic constitutive models on crack tip fields in steady crack growth. In: "Advances in Fracture Research," ed. D. Francois, Pergamon, Oxford, vol. 5, pp. 2607–2614.

P. Rahulkumar, A. Jagota, S. J. Bennison and S. Saigal, 2000, Cohesive element modeling of viscoelastic fracture: application to peel testing of polymers. *Int. J. Solids Struct.*, **37**, 1873–1897.

J. R. Rice, 1988, Elastic fracture concepts for interfacial cracks. *J. Appl. Mech.*, **55**, 98–103.

E. B. Saubestre, L. J. Durney, J. Haidu and E. Bastenbeck, 1965, The adhesion of electrodeposits to plastics. *Plating*, **52**, 982–1000.

G. J. Spies, 1953, The peeling test on redux-bonded joints. *J. Aircraft Eng.*, **25**, 64–70.

N. A. Stelmashenko, M. G. Walls, L. M. Brown and Y. V. Milman, 1993, Microindentations on W and Mo oriented single crystals: an STM study. *Acta Metall. Mater.*, **41**, 2855–2865.

J. S. Stolken and A. G. Evans, 1998, A microbend test method for measuring the plasticity length scale. *Acta Mater.*, **46**, 5109–5115.

T. Suga, G. Elssner and S. Schmauder, 1988, Composite parameters and mechanical compatibility of material joints. *J. Compos. Mater.*, **22**, 917–934.

Z. Suo, C. F. Shih and A. G. Varias, 1993, A theory for cleavage cracking in the presence of plastic flow. *Acta Metall. Mater.*, **41**, 1551–1557.

A. Tanaka, H. Kettunen, K. Niskanen and K. Keitaanniemi, 2000, Comparison of energy dissipation in the out-of-plane and in-plane fracture of paper. *J. Pulp Paper Sci.*, **26**, 385–390.

M. D. Thouless, 1990, Crack spacing in brittle films on elastic substrates. *J. Am. Ceram. Soc.*, **73**, 2144–2146.

M. D. Thouless, J. L. Adams, M. S. Kafkalidis, Y. Bankowski, R. A. Dickie and G. L. Westerbeek, 1998, Determining the toughness of plastically deforming joints. *J. Mater. Sci.*, **33**, 189–197.

M. D. Thouless, M. S. Kafkalidis, S. M. Ward, Y. Bankowski, R. A. Dickie and G. L. Westerbeek, 1997, Toughness of plastically-deforming asymmetric joints. *Scr. Mater.*, **37**, 1081–1087.

V. Tvergaard and J. W. Hutchinson, 1992, The relation between crack growth resistance and fracture process parameters in elastic–plastic solids. *J. Mech. Phys. Solids*, **40**, 1377–1397.

V. Tvergaard and J. W. Hutchinson, 1993, The influence of plasticity on mixed mode interface toughness. *J. Mech. Phys. Solids*, **41**, 1119–1135.

V. Tvergaard and J. W. Hutchinson, 1994, Toughness of an interface along a thin ductile layer joining elastic solids. *Phil. Mag. A*, **70**, 641–656.

J. S. Wang and Z. Suo, 1990, Experimental determination of interfacial toughness using Brazil-nut-sandwiches. *Acta Metall.*, **38**, 1279–1290.

Y. Wei, 2002, Thin layer splitting along the elastic–plastic solid surface. *Int. J. Fract.*, **113**, 233–252.

Y. Wei and J. W. Hutchinson, 1997a, Nonlinear delamination mechanics for thin films. *J. Mech. Phys. Solids*, **45**, 1137–1159.

Y. Wei and J. W. Hutchinson, 1997b, Steady-state crack growth and work of fracture for solids characterized by strain gradient plasticity. *J. Mech. Phys. Solids*, **45**, 1253–1273.

Y. Wei and J. W. Hutchinson, 1998, Interface strength, work of adhesion and plasticity in the peel test. *Int. J. Fract.*, **93**, 315–333.

Y. Wei and J. W. Hutchinson, 1999, Models of interface separation accompanied by plastic dissipation at multiple scales. *Int. J. Fract.*, **95**, 1–17.

Y. Wei, X. Wang, X. Wu and Y. Bai, 2001, Theoretical and experimental researches of size effect in micro-indentation test. *Sci. China A*, **44**, 74–82.

J. G. Williams, 1993, Root rotation and plastic work effects in the peel test. *J. Adhes.*, **41**, 225–239.

Q. D. Yang, M. D. Thouless and S. M. Ward, 1999, Numerical simulations of adhesively-bonded beams failing with extensive plastic deformation. *J. Mech. Phys. Solids*, **47**, 1337–1353.

Q. D. Yang, M. D. Thouless and S. M. Ward, 2000, Analysis of the symmetrical 90°-peel test with extensive plastic deformation. *J. Adhes.*, **72**, 115–132.

S. Yurenka, 1962, Peel testing of adhesive bonded metal. *J. Appl. Polym. Sci.*, **7**, 136–144.

Comprehensive Structural Integrity
ISBN (set): 0-08-043749-4
Volume 8; (ISBN: 0-08-044151-3); pp. 181–217